J. Fluid Mech. (2000), *vol.* 406, *pp.* 281–308. Printed in the United Kingdom

© 2000 Cambridge University Press

Nonlinear instability of plane liquid sheets

By SEYED A. JAZAYERI[1] AND XIANGUO LI[2]†

[1]Department of Mechanical Engineering, University of Victoria, Victoria, B.C., Canada V8W 3P6
[2] Department of Mechanical Engineering, University of Waterloo, Waterloo, Ontario, Canada N2L 3G1

(Received 24 July 1998 and in revised form 1 June 1999)

A nonlinear stability analysis has been carried out for plane liquid sheets moving in a gas medium at rest by a perturbation expansion technique with the initial amplitude of the disturbance as the perturbation parameter. The first, second and third order governing equations have been derived along with appropriate initial and boundary conditions which describe the characteristics of the fundamental, and the first and second harmonics. The results indicate that for an initially sinusoidal sinuous surface disturbance, the thinning and subsequent breakup of the liquid sheet is due to nonlinear effects with the generation of higher harmonics as well as feedback into the fundamental. In particular, the first harmonic of the fundamental sinuous mode is varicose, which causes the eventual breakup of the liquid sheet at the half-wavelength interval of the fundamental wave. The breakup time (or length) of the liquid sheet is calculated, and the effect of the various flow parameters is investigated. It is found that the breakup time (or length) is reduced by an increase in the initial amplitude of disturbance, the Weber number and the gas-to-liquid density ratio, and it becomes asymptotically insensitive to the variations of the Weber number and the density ratio when their values become very large. It is also found that the breakup time (or length) is a very weak function of the wavenumber unless it is close to the cut-off wavenumbers.

1. Introduction

Liquid sheet instability and subsequent breakup into ligaments and finally droplets are extensively utilized in many practical applications, ranging from spray drying operations, chemical and pharmaceutical processing, to power generation and propulsion systems (Lefebvre 1983; Masters 1985). A good understanding of the liquid sheet breakup process is essential for the design, operation and performance evaluation and improvement of the practical systems involved. As a result, numerous studies have been carried out to investigate various aspects of liquid sheet stability and breakup processes. A summary of the early studies related to the application of liquid atomization and sprays can be found in Lefebvre (1989).

The linear instability of a thin liquid sheet was investigated by Squire (1953) and Hagerty & Shea (1955), and both liquid and gas phases were taken as inviscid and incompressible. Hagerty & Shea (1955) showed that there can only exist two modes of unstable waves on the two gas–liquid interfaces for liquid sheets in a stationary gas medium, corresponding to the two surface waves oscillating exactly in and out of phase, commonly referred to as the sinuous and varicose modes,

† Author to whom correspondence should be addressed.

https://doi.org/10.1017/S0022112099007491 Published online by Cambridge University Press

and that the sinuous mode is always predominant under the typical conditions for practical applications. They also performed the first experimental measurements of the wave growth and wavelength for liquid sheets under various flow conditions, and the theoretical predictions were compared favourably with their experimental results. The effect of liquid viscosity was investigated by Li & Tankin (1991). It was shown that although aerodynamic instability dominates and the viscous effect reduces the wave growth rate for the sinuous mode at large Weber numbers and for the varicose mode at any Weber number, liquid viscosity can enhance the liquid sheet instability for the sinuous mode at low Weber numbers, and under this condition the viscosity-enhanced instability can even become predominant. Li (1994) also carried out a study on the stability of viscous liquid sheets in two gas streams of unequal velocities. It was found that two independent unstable modes exist for this case, named therein as para-sinuous and para-varicose modes, and they resemble, but certainly differ from, the well-known sinuous and varicose modes found by Hagerty & Shea (1955) for liquid sheets in a stationary gas medium. It was also shown that the relative velocities of the liquid and gas streams control the para-varicose mode and the para-sinuous mode at large Weber numbers, and the absolute velocities of the liquid and gas streams dominate the para-sinuous mode at small Weber numbers. The effect of gas compressibility on the liquid sheet instability has also been investigated by Li & Kelly (1992) for inviscid liquid sheets and by Cao & Li (1999) for viscous liquid sheets in two gas streams of unequal velocities. It was shown that gas compressibility always enhances the instability and breakup processes of liquid sheets. The absolute and spatial instability of liquid sheets has also been investigated (Lin, Lian & Creighton 1990; Li 1993), and reviewed by Li (1996). It was found that the absolute instability only occurs for the sinuous mode at small Weber numbers, approximately less than one, and the spatial and temporal instability are related to each other according to Gaster transformation (1962) for large Weber numbers of practical importance.

In all the above-cited theoretical studies, linearized stability analysis has been employed. The linear theory does not offer a means for the liquid sheet to break up, because during the growth of the sinuous mode of disturbances predominant under practical conditions, the two gas–liquid interfaces remain a constant distant apart. Hence, the liquid sheet breakup length, which is an important parameter in the spray modelling and spray system design, cannot be predicted based on the linear theory alone. In reality, the liquid sheet breakup processes are nonlinear, especially near the breakup region, as observed experimentally (Mansour & Chigier 1990; Hashimoto & Suzuki 1991). So far, only limited studies have been carried out on the nonlinearity of the liquid sheet breakup processes. Clark & Dombrowski (1972) were the first to analyse nonlinear liquid sheet disintegration through the perturbation expansion technique with initial disturbance amplitude as the perturbation parameter. A solution accurate up to the second order of the initial disturbance amplitude was obtained for the case of wavelengths relatively long compared with the sheet thickness. It was found that sheet thinning was caused by the growth of the harmonic wave, with maximum thinning and subsequent rupture occurring at positions corresponding to 3/8 and 7/8 of the length of the fundamental wave. The theoretical results were also used to calculate the breakup lengths of attenuating liquid sheets produced by fan and swirl spray nozzles, and compared with experimental measurements. Rangel & Sirignano (1988) used the vortex-sheet discretization method and computation technique to investigate the nonlinear evolution of initially small disturbances at an interface separating two fluids of different density and velocity with effects of surface tension included. The same approach was also used in a later study (Rangel

https://doi.org/10.1017/S0022112099007491 Published online by Cambridge University Press

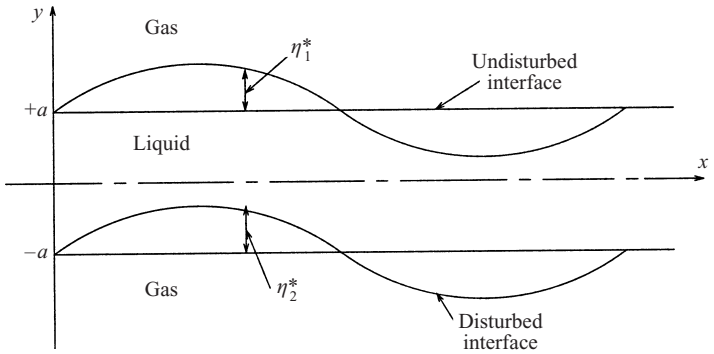


FIGURE 1. Schematic of a plane liquid sheet and sinuous disturbance.

& Sirignano 1991) for the linear and nonlinear instability of a finite-thickness fluid sheet in contact with two semi-infinite streams of a different fluid. It was shown that sinuous disturbances may result in the formation of ligaments interspaced at half the wavelength of the fundamental mode.

On the other hand, the nonlinear breakup for a similar problem, namely a circular liquid jet in the Rayleigh breakup regime, has been studied extensively, through either perturbation expansion (Yuen 1968), one-dimensional approximation (Bogy 1978) or numerical simulation (Ashgriz & Mashayek 1995). Experimental investigation by Taub (1976) indicates that for the breakup of circular liquid jets, the closer to the breakup region, the higher the order of the nonlinear perturbation analysis has to be in order for adequate description of the breakup behaviour. Both theoretical and experimental studies were reviewed up to 1979 by Bogy (1979), who pointed out that the perturbation solutions are capable of describing the process of liquid jet breakup and satellite-drop formation, and a nonlinear analysis up to the third order of perturbation expansion in terms of the initial disturbance amplitude is generally sufficient to account for the inherent nonlinear nature of the breakup process. Therefore, a third-order nonlinear analysis has been carried out in this study with the initial amplitude as the expansion parameter. The objectives are to investigate the process of liquid sheet disruption preceding spray droplet formation, the effect of finite amplitude of the disturbance on the development of the surface wave-forms, and the effect of various flow parameters on the liquid sheet breakup process, and to calculate the liquid sheet breakup length as a function of various flow parameters.

2. Mathematical formulation

A two-dimensional liquid sheet of thickness $2a$ is considered, as schematically shown in figure 1. The liquid is Newtonian with a density ρ_l, and the liquid sheet moves at a uniform axial velocity of U_l in a stationary surrounding gas medium of density ρ_g. Both liquid and gas phases are assumed inviscid and incompressible, and the effect of gravity is neglected here because the Froude number is typically very large for practical liquid atomization and sprays. Although liquid viscosity, as shown by Li & Tankin (1991), introduces an additional mode which destabilizes a range of wavenumbers at small Weber numbers, its effect at large Weber numbers, typical of atomization and spray application, is primarily in reducing the disturbance growth rate and increasing the dominant wavelength. Therefore, for simplicity and with no loss of generality, liquid viscosity is neglected in this study. Gas viscosity is neglected

https://doi.org/10.1017/S0022112099007491 Published online by Cambridge University Press

because of the observation that it is only weakly stabilizing, and does not influence the relevant phenomenon appreciably, as Lin & Ibrahim (1990) found in a related work. The velocity of the gas streams on both sides of the liquid sheet can have significant and complex effects on the characteristics of the surface waves as shown by Li (1994) in his linear analysis. Hence, the gas velocity is avoided in this first attempt at the nonlinear effect, and will be examined in a further work on nonlinear breakup of liquid sheets.

For the purpose of analysis, we shall assume that the liquid flow is initially irrotational and the gas motion starts from rest so that the flow field can be treated as potential flow because of the inviscid assumption. For such a flow situation, the pressure field is constant within the liquid and the gas phase, and there is no discontinuity across the two liquid–gas interfaces due to the effect of surface tension, which is denoted by σ, because of the infinite radius of curvature of the plane surface.

When disturbances set in, the interfacial deformation of the liquid sheet results, and the upper and lower interfaces are now located at $y = a+\eta_1^*(x,t)$ and $y = -a+\eta_2^*(x,t)$, respectively. Correspondingly, the flow field is disturbed and deviates from the base flow field described above. For proper presentation of the analysis and interpretation of the results, all physical parameters are non-dimensionalized. The length, time, and density are scaled by the half-sheet thickness a, the convection time a/U_l, and the liquid density ρ_l. Then for the Cartesian coordinate system defined in figure 1, where the x-axis lies at the centreline of the undisturbed sheet in the direction of the liquid flow, the dimensionless velocity potential ϕ for the gas and liquid phases, and the dimensionless surface disturbance η_j in the y-direction must satisfy the following governing equations and boundary conditions:

governing equations

$$\phi_{g,xx} + \phi_{g,yy} = 0 \quad \text{for } 1+\eta_1 \leqslant y < +\infty, \quad -\infty < y \leqslant -1+\eta_2, \tag{1}$$

$$\phi_{l,xx} + \phi_{l,yy} = 0 \quad \text{for } -1+\eta_2 \leqslant y \leqslant 1+\eta_1; \tag{2}$$

boundary conditions

$$\phi_{l,y} - \eta_{j,t} - \phi_{l,x}\eta_{j,x} = 0, \tag{3}$$

$$\phi_{g,y} - \eta_{j,t} - \phi_{g,x}\eta_{j,x} = 0, \tag{4}$$

$$\tfrac{1}{2} + \rho\phi_{g,t} - \phi_{l,t} + \tfrac{1}{2}\rho(\phi_{g,x}^2 + \phi_{g,y}^2) - \tfrac{1}{2}(\phi_{l,x}^2 + \phi_{l,y}^2) = \frac{(-1)^j}{We}\frac{\eta_{j,xx}}{(1+\eta_{j,x}^2)^{3/2}}, \tag{5}$$

which are valid at $y = (-1)^{j+1} + \eta_j$, and $j = 1$ represents the upper interface and $j = 2$ the lower interface. In the above equations, the dimensionless Weber number and the gas density (or the gas-to-liquid density ratio) are defined as

$$We = \frac{\rho_l U_l^2 a}{\sigma}, \qquad \rho = \frac{\rho_g}{\rho_l}. \tag{6}$$

Equations (3) and (4) represent the kinematic boundary condition – the gas–liquid interfaces are material surfaces, and the fluid particles initially on the interfaces will remain there subsequently. Equation (5) is the dynamic boundary condition, stating that the difference in the normal stresses across the interfaces is balanced by the surface tension forces. In order to solve the above equations subject to the boundary conditions given, an initial condition must be specified as well. The initial condition can commonly be in the form of surface, pressure or velocity disturbances or any combinations among them. Since the following development does not require

https://doi.org/10.1017/S0022112099007491 Published online by Cambridge University Press

a knowledge of the specific forms of the initial condition, we shall defer the statement of the initial condition until the solution section later on. It only suffices to state here that the initial disturbance has a characteristic amplitude η_0, which is an independent variable in the following perturbation analysis and can be measured in laboratory experiments as in Asare, Takahashi & Hoffman (1981).

In the present study, we shall seek solutions to the governing equations with the boundary conditions by using a perturbation expansion technique with the initial disturbance amplitude η_0 as the perturbation parameter. Hence it is assumed that the location of the two gas–liquid interfaces can be expressed as follows:

$$\eta_j = \sum_{n=1}^{\infty} \eta_0^n \eta_{jn}(x,t). \tag{7}$$

If η_{jn} and all its derivatives can be considered to have the same order of magnitude, then it is evident from (3) and (4) that the velocity potential for the liquid and gas phases takes the following form:

$$\phi_l = \sum_{n=0}^{\infty} \eta_0^n \phi_{ln}(x,y,t), \tag{8}$$

$$\phi_g = \sum_{n=1}^{\infty} \eta_0^n \phi_{gn}(x,y,t), \tag{9}$$

where $\phi_{l0} = x$ represents the normalized base flow field.

Because the governing equations, (1) and (2), are linear, they must be satisfied by each of the ϕ_{ln} and ϕ_{gn} independently. The corresponding boundary conditions for each order of η_0^n are determined by substituting (7)–(9) into (3)–(5), and equating the coefficients of the same power of η_0^n. Note that since the interfacial location $\eta_j(x,t)$ is a part of the solution, and not known *a priori*, the velocity potentials ϕ_{ln} and ϕ_{gn} evaluated at $y = (-1)^{j+1} + \eta_j$ are approximated by a Taylor series expansion around $y = (-1)^{j+1}$

$$\phi|_{y=(-1)^{j+1}+\eta_j} = \phi|_{y=(-1)^{j+1}} + \eta_j \phi_{,y|y=(-1)^{j+1}} + \frac{\eta_j^2}{2!}\phi_{,yy|y=(-1)^{j+1}} + \frac{\eta_j^3}{3!}\phi_{,yyy|y=(-1)^{j+1}} + \cdots, \tag{10}$$

where η_j is given in (7). Thus the obtained boundary conditions are now linear at each order of the approximation, and all nonlinear terms involved contain lower-order solutions which at any given order will have been solved and known. Hence, in principle successively higher orders can be solved to yield solutions that are progressively more accurate.

As discussed in the introduction, this study will only solve the first three orders for the governing equations and corresponding boundary conditions which are evaluated at the unperturbed interfaces $y = (-1)^{j+1}$. They are given below, after lengthy algebraic manipulations:

η_0 (or the first) order

$$\phi_{g1,xx} + \phi_{g1,yy} = 0 \quad \text{for } +1 \leqslant y < +\infty, \text{ and } -\infty < y \leqslant -1, \tag{11}$$

$$\phi_{l1,xx} + \phi_{l1,yy} = 0 \quad \text{for } -1 \leqslant y \leqslant +1, \tag{12}$$

$$\phi_{l1,y} - \eta_{j1,t} - \eta_{j1,x} = 0, \tag{13}$$

https://doi.org/10.1017/S0022112099007491 Published online by Cambridge University Press

$$\phi_{g1,y} - \eta_{j1,t} = 0, \tag{14}$$

$$\rho\phi_{g1,t} - \phi_{l1,t} - \phi_{l1,x} - (-1)^j \frac{\eta_{j1,xx}}{We} = 0; \tag{15}$$

η_0^2 (or the second) order

$$\phi_{g2,xx} + \phi_{g2,yy} = 0 \quad \text{for } +1 \leqslant y < +\infty, \text{ and } -\infty < y \leqslant -1, \tag{16}$$

$$\phi_{l2,xx} + \phi_{l2,yy} = 0 \quad \text{for } -1 \leqslant y \leqslant +1, \tag{17}$$

$$\phi_{l2,y} - \eta_{j2,t} - \eta_{j2,x} = -\eta_{j1}\phi_{l1,yy} + \eta_{j1,x}\phi_{l1,x}\,, \tag{18}$$

$$\phi_{g2,y} - \eta_{j2,t} = -\eta_{j1}\phi_{g1,yy} + \eta_{j1,x}\phi_{g1,x}\,, \tag{19}$$

$$\begin{aligned}\rho\phi_{g2,t} - \phi_{l2,t} - \phi_{l2,x} - (-1)^j \frac{\eta_{j2,xx}}{We} &= -\rho[\eta_{j1,t}\phi_{g1,y} + \eta_{j1}\phi_{g1,yt}] + [\eta_{j1,t}\phi_{l1,y} + \eta_{j1}\phi_{l1,yt}] \\ &\quad -\tfrac{1}{2}\rho(\phi_{g1,x}^2 + \phi_{g1,y}^2) + \tfrac{1}{2}(\phi_{l1,x}^2 + \phi_{l1,y}^2) + [\eta_{j1,x}\phi_{l1,y} + \eta_{j1}\phi_{l1,xy}];\end{aligned} \tag{20}$$

η_0^3 (or the third) order

$$\phi_{g3,xx} + \phi_{g3,yy} = 0 \quad \text{for } +1 \leqslant y < +\infty, \text{ and } -\infty < y \leqslant -1, \tag{21}$$

$$\phi_{l3,xx} + \phi_{l3,yy} = 0 \quad \text{for } -1 \leqslant y \leqslant +1, \tag{22}$$

$$\begin{aligned}\phi_{l3,y} - \eta_{j3,t} - \eta_{j3,x} = &-\eta_{j2}\phi_{l1,yy} - \eta_{j1}\phi_{l2,yy} - \tfrac{1}{2}\eta_{j1}^2\phi_{l1,yyy} + \eta_{j1,x}\phi_{l2,x} \\ &+\eta_{j2,x}\phi_{l1,x} + \eta_{j1}\phi_{l1,xy}\eta_{j1,x},\end{aligned} \tag{23}$$

$$\begin{aligned}\phi_{g3,y} - \eta_{j3,t} = &-\eta_{j2}\phi_{g1,yy} - \eta_{j1}\phi_{g2,yy} - \tfrac{1}{2}\eta_{j1}^2\phi_{g1,yyy} + \eta_{j1,x}\phi_{g2,x} \\ &+\eta_{j2,x}\phi_{g1,x} + \eta_{j1}\phi_{g1,xy}\eta_{j1,x},\end{aligned} \tag{24}$$

$$\begin{aligned}&\rho\phi_{g3,t} - \phi_{l3,t} - \phi_{l3,x} - (-1)^j \frac{\eta_{j3,xx}}{We} \\ &= -\rho[\eta_{j1,t}\phi_{g2,y} + \eta_{j1}\phi_{g2,yt} + \eta_{j2,t}\phi_{g1,y} + \eta_{j2}\phi_{g1,yt} + \eta_{j1}\eta_{j1,t}\phi_{g1,yy} + \tfrac{1}{2}\eta_{j1}^2\phi_{g1,yyt}] \\ &\quad +[\eta_{j1,t}\phi_{l2,y} + \eta_{j1}\phi_{l2,yt} + \eta_{j2,t}\phi_{l1,y} + \eta_{j2}\phi_{l1,yt} + \eta_{j1}\eta_{j1,t}\phi_{l1,yy} + \tfrac{1}{2}\eta_{j1}^2\phi_{l1,yyt}] \\ &\quad -\rho[\phi_{g1,x}(\phi_{g2,x} + \eta_{j1,x}\phi_{g1,y} + \eta_{j1}\phi_{g1,xy}) + \phi_{g1,y}(\phi_{g2,y} + \eta_{j1,y}\phi_{g1,y} + \eta_{j1}\phi_{g1,yy})] \\ &\quad +[\phi_{l1,x}(\phi_{l2,x} + \eta_{j1,x}\phi_{l1,y} + \eta_{j1}\phi_{l1,xy}) + \phi_{l1,y}(\phi_{l2,y} + \eta_{j1,y}\phi_{l1,y} + \eta_{j1}\phi_{l1,yy}) \\ &\quad +(\eta_{j1,x}\phi_{l2,y} + \eta_{j1}\phi_{l2,xy} + \eta_{j2,x}\phi_{l1,y} + \eta_{j2}\phi_{l1,xy} + \eta_{j1}\eta_{j1,x}\phi_{l1,yy} + \tfrac{1}{2}\eta_{j1}^2\phi_{l1,xyy})] \\ &\quad -\frac{3(-1)^j}{2We}\eta_{j1,xx}\eta_{j1,x}^2\,.\end{aligned} \tag{25}$$

3. Solution

In order to solve the governing equations subject to the boundary conditions given in the previous section for the first three orders, an initial condition must be specified. In practice, surface deformation can develop from surface, velocity or pressure disturbances or a combination imposed initially on the flow field. Although the first-order solution will remain the same, regardless of the initial form of disturbances imposed, the higher orders of solution will depend sensitively on the initial condition. For the present study, we shall assume that the surface deformation is due initially to a sinusoidal surface wave with amplitude η_0 and wavenumber k. For liquid sheets in a stationary gas medium, it is known (Squire 1953; Hagerty & Shea 1955; Li &

https://doi.org/10.1017/S0022112099007491 Published online by Cambridge University Press

Tankin 1991) that the surface waves on the two gas–liquid interfaces can propagate exactly in or out of phase, called sinuous or varicose waves, and the sinuous waves are always more unstable than the corresponding varicose waves under the practically important flow conditions. Therefore, the present study will only seek solution for the development of sinuous waves and the consequent breakup of the liquid sheet.

The first-order solution is determined from the following initial condition:

$$\eta_{j1}(x,0) = \cos(kx); \quad \text{and} \quad \eta_{j1,t}(x,0) = -\alpha_1 \sin(kx), \tag{26}$$

where k is the dimensionless wavenumber of the disturbance and is related to the wavelength λ by $k = 2\pi/\lambda$, and it is the same as the linearized analysis of Squire (1953), Hagerty & Shea (1955), and Li & Tankin (1991). The results are given below for the completeness of the presentation:

$$\phi_{l1} = \frac{\sinh(ky)}{\cosh(k)}\left[\left(\frac{\psi_{j1,t}}{k} + \mathrm{i}\psi_{j1}\right)\exp(\mathrm{i}kx) + \left(\frac{\overline{\psi}_{j1,t}}{k} - \mathrm{i}\overline{\psi}_{j1}\right)\exp(-\mathrm{i}kx)\right], \tag{27}$$

$$\phi_{g1} = (-1)^j\left[\frac{\psi_{j1,t}}{k}\exp(\mathrm{i}kx) + \frac{\overline{\psi}_{j1,t}}{k}\exp(-\mathrm{i}kx)\right]\exp[k + (-1)^j ky], \tag{28}$$

$$\eta_{j1} = \psi_{j1}\exp(\mathrm{i}kx) + \overline{\psi}_{j1}\exp(-\mathrm{i}kx), \tag{29}$$

where the amplitude of the surface disturbance is

$$\psi_{j1} = \tfrac{1}{2}\cosh(\beta_1 t)\exp(\mathrm{i}\alpha_1 t) \tag{30}$$

and α_1 and β_1 are the real and imaginary parts of the complex frequency ω_1 $(= \alpha_1 + \mathrm{i}\beta_1)$ and its complex conjugate $\overline{\omega_1}$ $(= \alpha_1 - \mathrm{i}\beta_1)$, and are given as follows:

$$\alpha_1 = -\frac{k\tanh(k)}{\tanh(k) + \rho}, \tag{31}$$

$$\beta_1 = \pm\frac{k\{\rho\tanh(k) - [\tanh(k) + \rho]k/We\}^{1/2}}{\tanh(k) + \rho}. \tag{32}$$

It is clear that (29) indicates that the first-order surface deformation η_{j1} is the same for the upper $(j = 1)$ and lower $(j = 2)$ interfaces, hence it represents a sinuous wave, as we initially set out to find. The above solutions show that if the wavenumber k is such that for a given flow condition (i.e. fixed ρ and We) $\rho\tanh(k) - [\tanh(k) + \rho]k/We > 0$, then β_1 is real, and the surface waves grow. For $\rho\tanh(k) - [\tanh(k) + \rho]k/We < 0$, β_1 is purely imaginary, and the surface waves oscillate. The pure oscillation without decay for this case is due to the assumption of inviscid fluids (Li & Tankin, 1991), because viscous effects are stabilizing for short-wavelength disturbances and decrease the disturbance energy (Li 1994), hence resulting in the oscillation of surface waves with a decaying amplitude. Therefore, the wavenumber k corresponding to $\rho\tanh(k) - [\tanh(k) + \rho]k/We = 0$ represents the cut-off wavenumber k_c, which divides the wavenumber spectrum into a region of stable travelling waves and a region of exponentially growing waves with an optimum wavenumber that corresponds to the fastest growing wave. This optimum wavenumber is often referred to as the dominant wavenumber.

https://doi.org/10.1017/S0022112099007491 Published online by Cambridge University Press

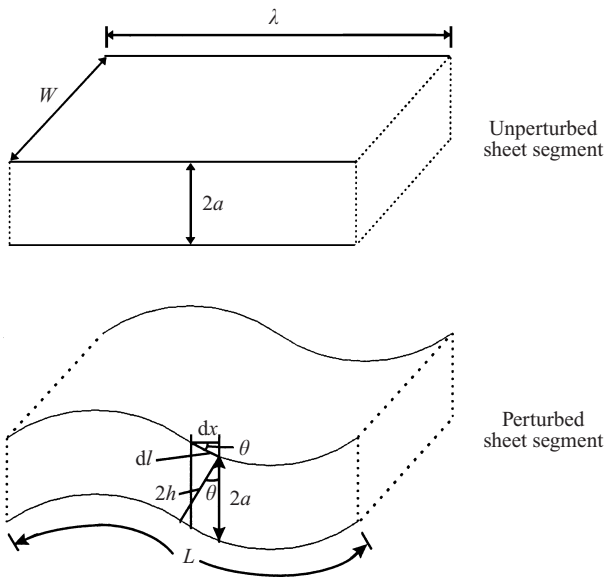


FIGURE 2. Schematic of a planar and a sinuously perturbed liquid sheet for the analysis of conservation of liquid mass.

It should be pointed out that concern has been raised (Spielbauer & Aidun 1994) as to whether the first-order solution (i.e. the linearized analysis) satisfies the conservation of mass for the liquid phase. Consider a planar liquid sheet segment of one wavelength λ long and an arbitrary width W, as illustrated in figure 2. For the sake of discussion in this paragraph, variables used are dimensional quantities. The unperturbed sheet has a uniform thickness of $2a$ (the distance between two interfaces in the vertical direction), and the mass contained within this segment, m_u, is then

$$m_u = \rho_l W(2a)\lambda. \tag{33}$$

For the sinuously perturbed sheet, the mass contained within the distance of one wavelength in the flow direction, m_p, is

$$m_p = \int_0^L \rho_l W(2h)\,\mathrm{d}l, \tag{34}$$

where L is the length of the sinuously perturbed sheet segment as measured along the deformed surface of the sheet, $\mathrm{d}l$ is the corresponding differential length, and $2h$ is the distance between the two interfaces normal to the deformed surface, as shown in figure 2. It should be emphasized that the distance between the two interfaces in the vertical direction remains unchanged, i.e. $2a$, because the two interfaces are displaced in the same direction by exactly the same amount by the sinuous waves. However, the normal distance, $2h$, is not a constant, rather it varies along the deformed sheet, depending on the local curvature of the sheet and it reaches the maximum value of $2a$ at the wave crests and troughs. From the geometrical relation shown in figure 2, we have

$$\mathrm{d}l = \frac{\mathrm{d}x}{\cos\theta}, \qquad 2h = (2a)\cos\theta. \tag{35}$$

https://doi.org/10.1017/S0022112099007491 Published online by Cambridge University Press

Now substitution of (35) into (34) results in

$$\begin{aligned} m_p &= \int_0^{\lambda} \rho_l W[(2a)\cos\theta]\left(\frac{\mathrm{d}x}{\cos\theta}\right) \\ &= \int_0^{\lambda} \rho_l W(2a)\,\mathrm{d}x \\ &= \rho_l W(2a)\lambda \\ &= m_u. \end{aligned} \tag{36}$$

Hence, the liquid mass is conserved before and after the sinuous waves set in. To demonstrate the mass conservation from another perspective, consider the perturbed liquid sheet surfaces to be represented by the following equations (Li & Tankin 1991), as shown in figure 1:

$$y_1 = +a + \eta_1^* \quad \text{for the upper surface,} \tag{37}$$

$$y_2 = -a + \eta_2^* \quad \text{for the lower surface.} \tag{38}$$

The mass contained within one wavelength λ is then

$$\begin{aligned} m_p &= \int_0^{\lambda} \rho_l W(y_1 - y_2)\,\mathrm{d}x \\ &= \int_0^{\lambda} \rho_l W[2a + (\eta_1^* - \eta_2^*)]\,\mathrm{d}x. \end{aligned} \tag{39}$$

For the sinuously perturbed sheet, $\eta_1^* = \eta_2^*$. Therefore, the above integral yields $m_p = \rho_l W(2a)\lambda = m_u$. This method can be easily utilized to show that the higher-order solutions obtained later in this study satisfy the conservation of mass as well.

For the second-order solution, we shall assume that the surface deformation is in the following form:

$$\eta_{j2} = \psi_{j2}\exp(2\mathrm{i}kx) + \overline{\psi}_{j2}\exp(-2\mathrm{i}kx) \tag{40}$$

with the initial condition

$$\eta_{j2}(x,0) = 0 \quad \text{and} \quad \eta_{j2,t}(x,0) = 0. \tag{41}$$

Substituting (40) into (18) and (19), respectively, along with the known first-order solutions suggests the following form for the velocity potentials for the liquid and gas phases:

$$\phi_{l2} = f_{l2}(y)[a_{22}(t)\exp(2\mathrm{i}kx) + \overline{a}_{22}(t)\exp(-2\mathrm{i}kx)] + A_{l2}(t), \tag{42}$$

$$\phi_{g2} = f_{g2}(y)[b_{22}(t)\exp(2\mathrm{i}kx) + \overline{b}_{22}(t)\exp(-2\mathrm{i}kx)] + A_{g2}(t). \tag{43}$$

The unknown functions of y can be determined by substituting the above equations into the governing equations, (16) and (17), and the time dependence can be obtained from the kinematic and dynamic boundary conditions, (18)–(20), and the initial conditions, (41). After considerable effort, the velocity potentials for the liquid and gas phases are determined as follows:

$$\begin{aligned} \phi_{l2} = -\frac{\cosh(2ky)}{(2k)\sinh(2k)}\Bigg\{ &\left[2k^2\tanh(k)\left(\frac{\psi_{j1}\psi_{j1,t}}{k} + \mathrm{i}\psi_{j1}^2\right) + \psi_{j2,t} + 2\mathrm{i}k\psi_{j2}\right]_{j=2}\exp(2\mathrm{i}kx) \\ &+ \left[2k^2\tanh(k)\left(\frac{\overline{\psi}_{j1}\overline{\psi}_{j1,t}}{k} - \mathrm{i}\overline{\psi}_{j1}^2\right) + \overline{\psi}_{j2,t} - 2\mathrm{i}k\overline{\psi}_{j2}\right]_{j=2}\exp(-2\mathrm{i}kx)\Bigg\} + A_{l2}(t), \end{aligned} \tag{44}$$

https://doi.org/10.1017/S0022112099007491 Published online by Cambridge University Press

$$\phi_{g2} = -\frac{\exp[2k + (-1)^j 2ky]}{2k}[(-(-1)^j \psi_{j2,t} + 2k\psi_{j1}\psi_{j1,t})\exp(2ikx) + (-(-1)^j \overline{\psi}_{j2,t} + 2k\overline{\psi}_{j1}\overline{\psi}_{j1,t})\exp(-2ikx)] + A_{g2}(t), \quad (45)$$

where a line over a variable denotes the complex conjugate of that variable, the temporal part of the disturbance amplitude is given

$$\psi_{j2} = (-1)^j[A_1 \exp(i\omega_2 t) + \overline{A}_1 \exp(i\overline{\omega}_2 t) + A_2 \exp(2i\omega_1 t) + \overline{A}_2 \exp(2i\overline{\omega}_1 t) + A_3 \exp(2i\alpha_1 t)], \quad (46)$$

and the second-order complex temporal frequency is

$$\omega_2 = \alpha_2 + i\beta_2, \quad (47)$$

where

$$\left.\begin{aligned} \alpha_2 &= -\frac{(2k)\coth(2k)}{\coth(2k) + \rho}, \\ \beta_2 &= \pm\frac{(2k)\{\rho\coth(2k) - [\coth(2k) + \rho](2k)/We\}^{1/2}}{\coth(2k) + \rho}. \end{aligned}\right\} \quad (48)$$

The purely time-dependent functions $A_{l2}(t)$ and $A_{g2}(t)$, and the integration constants A_1, A_2, and A_3 are given in Appendix A.

The equation for the surface deformation, η_{j2}, indicates that the growth of the first harmonic contributes to the liquid sheet breakup, and the liquid mass is conserved up to the second order, in contrast with the Rayleigh breakup of circular liquid jets (Yuen 1968). It is also noticed that η_{j2} has the same magnitude, but opposite sign for the upper ($j = 1$) and lower ($j = 2$) interfaces. Coupled with (47)–(48), it is clear that the second-order surface disturbance is varicose in nature. Therefore, during the wave growth the two interfaces will not keep the same distance apart due to the growth of the first-harmonic varicose disturbance. The velocity potential for the liquid and gas phases includes the growth of the first harmonic and a purely time-dependent term which arises from the acceleration of the fluid. Similar to the Rayleigh breakup of circular liquid jets (Yuen 1968), the growth of the first harmonic is due to two effects. One is the feeding of energy from the fundamental as shown by the terms having a growth rate of $2\omega_1$ and $2\overline{\omega}_1$, and the other is due to the inherent instability of the first harmonic of the varicose disturbances itself when the dimensionless wavenumber $2k$ is such that $\rho\coth(2k) - [\coth(2k) + \rho](2k)/We > 0$. The latter is quite different from the Rayleigh breakup (Yuen 1968) where both the first harmonic and the fundamental have the same wave characteristics, that is, they both belong to the varicose disturbances.

For the third-order approximation, substitution of the first- and second-order solutions into the boundary conditions, (23) and (24), suggests that the surface disturbance should be sought in the following form:

$$\eta_{j3} = \psi_{j3}(t)\exp(3ikx) + \overline{\psi}_{j3}(t)\exp(-3ikx) + \Psi_{j3}(t)\exp(ikx) + \overline{\Psi}_{j3}(t)\exp(-ikx) \quad (49)$$

and the initial condition for the present problem is

$$\eta_{j3}(x, 0) = 0 \quad \text{and} \quad \eta_{j3,t}(x, 0) = 0. \quad (50)$$

With (49), the kinematic boundary conditions indicate that the velocity potentials for the liquid and gas phase should be sought in the following form:

$$\phi_{l3} = f_{l31}(y)[a_{31}(t)\exp(ikx) + \overline{a}_{31}(t)\exp(-ikx)] + f_{l33}(y)[a_{33}(t)\exp(3ikx) + \overline{a}_{33}(t)\exp(-3ikx)] + B_{l3}(t), \quad (51)$$

https://doi.org/10.1017/S0022112099007491 Published online by Cambridge University Press

$$\phi_{g3} = f_{g31}(y)[b_{31}(t)\exp(\mathrm{i}kx) + \bar{b}_{31}(t)\exp(-\mathrm{i}kx)] + f_{g33}(y)[b_{33}(t)\exp(3\mathrm{i}kx) + \bar{b}_{33}(t)\exp(-3\mathrm{i}kx)] + B_{g3}(t). \quad (52)$$

Substituting the above two equations into (22) and (21) leads to expressions for the y dependence with unknown integration constants. These constants and the time-dependent coefficients a, b and B are obtained from the boundary and initial conditions, similar to the second-order solution. It turns out that $\rho B_{g3} - B_{l3} = \text{constant}$, and hence both B_{g3} and B_{l3} can be neglected without any effect on the resulting flow field or on the balance of the normal stresses at the two boundaries. The final solution for the third order then becomes

$$\phi_{l3} = \frac{\sinh(ky)}{k\cosh(k)}[a_{31}(t)\exp(\mathrm{i}kx) + \bar{a}_{31}(t)\exp(-\mathrm{i}kx)] + \frac{\sinh(3ky)}{(3k)\cosh(3k)}[a_{33}(t)\exp(3\mathrm{i}kx) + \bar{a}_{33}(t)\exp(-3\mathrm{i}kx)], \quad (53)$$

$$\phi_{g3} = (-1)^j\frac{\exp[k + (-1)^j ky]}{k}[b_{31}(t)\exp(\mathrm{i}kx) + \bar{b}_{31}(t)\exp(-\mathrm{i}kx)] + (-1)^j\frac{\exp[(3k) + (-1)^j(3k)y]}{(3k)}[b_{33}(t)\exp(3\mathrm{i}kx) + \bar{b}_{33}(t)\exp(-3\mathrm{i}kx)], \quad (54)$$

where the time-dependent coefficients a and b are given in Appendix B, and the temporal part of the amplitude of surface disturbance is

$$\begin{aligned}\psi_{j3} = {} & D_1\exp(\mathrm{i}\omega_3 t) + \overline{D}_1\exp(\mathrm{i}\overline{\omega}_3 t) + D_2\exp[\mathrm{i}(\omega_1+\omega_2)t] + \overline{D}_2\exp[\mathrm{i}(\overline{\omega}_1+\overline{\omega}_2)t] \\ & + D_3\exp[\mathrm{i}(\omega_1+\overline{\omega}_2)t] + \overline{D}_3\exp[\mathrm{i}(\overline{\omega}_1+\omega_2)t] + D_4\exp[\mathrm{i}(\omega_1+2\overline{\omega}_1)t] \\ & + \overline{D}_4\exp[\mathrm{i}(\overline{\omega}_1+2\omega_1)t] + D_5\exp(\mathrm{i}3\omega_1 t) + \overline{D}_5\exp(\mathrm{i}3\overline{\omega}_1 t) \\ & + D_6\exp[\mathrm{i}(\omega_1+2\alpha_1)t] + \overline{D}_6\exp[\mathrm{i}(\overline{\omega}_1+2\alpha_1)t], \end{aligned} \quad (55)$$

$$\begin{aligned}\Psi_{j3} = {} & F_1\exp(\mathrm{i}\omega_1 t) + \overline{F}_1\exp(\mathrm{i}\overline{\omega}_1 t) + F_2\exp[\mathrm{i}(\omega_2-\omega_1)t] + \overline{F}_2\exp[\mathrm{i}(\overline{\omega}_2-\overline{\omega}_1)t] \\ & + F_3\exp[\mathrm{i}(\omega_2-\overline{\omega}_1)t] + \overline{F}_3\exp[\mathrm{i}(\overline{\omega}_2-\omega_1)t] + F_4\exp[\mathrm{i}(2\omega_1-\overline{\omega}_1)t] \\ & + \overline{F}_4\exp[\mathrm{i}(2\overline{\omega}_1-\omega_1)t] + F_5\exp[\mathrm{i}(\omega_1-\overline{\omega}_1)t] + \overline{F}_5\exp[\mathrm{i}(\overline{\omega}_1-\omega_1)t] \\ & + F_6\exp[\mathrm{i}(2\alpha_1-\omega_1)t] + \overline{F}_6\exp[\mathrm{i}(2\alpha_1-\overline{\omega}_1)t] + F_7, \end{aligned} \quad (56)$$

where the third-order complex temporal frequency is

$$\omega_3 = \alpha_3 + \mathrm{i}\beta_3, \quad (57)$$

$$\alpha_3 = -\frac{(3k)\tanh(3k)}{\tanh(3k)+\rho}, \quad (58)$$

$$\beta_3 = \pm\frac{(3k)\{\rho\tanh(3k) - [\tanh(3k)+\rho](3k)/We\}^{1/2}}{\tanh(3k)+\rho}, \quad (59)$$

and the constants of integration, D and F, are given in Appendix B.

The above third-order solution indicates that η_{j3} is the same for both the upper and lower interfaces since $\psi_{13} = \psi_{23}$ and $\Psi_{13} = \Psi_{23}$. Therefore, the third-order surface deformation is sinuous in nature, in contrast to the second-order one which is varicose. It is also noticed that the liquid mass is conserved up to the third order. As a result of the interaction among the lower harmonics, not only a higher harmonic ($\exp(3\mathrm{i}kx)$ and $\exp(-3\mathrm{i}kx)$) appears, but there also exists a feedback into the fundamental

https://doi.org/10.1017/S0022112099007491 Published online by Cambridge University Press

($\exp(\mathrm{i}kx)$ and $\exp(-\mathrm{i}kx)$) for the velocity potentials for both the liquid and gas phases, as well as for the surface deformation. Similar to the first harmonic, the growth of the second harmonic is due to two effects: the direct feeding of energy from the lower harmonics, and the inherent instability of the second harmonic itself when the dimensionless wavenumber satisfies the following condition:

$$\rho \tanh(3k) - [\tanh(3k) + \rho](3k)/We > 0. \tag{60}$$

Hence, the expression for the evolution of the two gas–liquid interfaces for an initial harmonic surface disturbance is, up to the third order

$$\begin{aligned}\eta_j &= \sum_{n=0}^{\infty} \eta_0^n \eta_{jn} \\ &= \eta_0[\psi_{j1}\exp(\mathrm{i}kx) + \overline{\psi}_{j1}\exp(-\mathrm{i}kx)] + \eta_0^2[\psi_{j2}\exp(2\mathrm{i}kx) + \overline{\psi}_{j2}\exp(-2\mathrm{i}kx)] \\ &\quad + \eta_0^3[\psi_{j3}\exp(3\mathrm{i}kx) + \overline{\psi}_{j3}\exp(-3\mathrm{i}kx) + \Psi_{j3}(t)\exp(\mathrm{i}kx) + \overline{\Psi}_{j3}(t)\exp(-\mathrm{i}kx)].\end{aligned} \tag{61}$$

This expression can be re-written in terms of a complex Fourier series as

$$\eta_j = \sum_{n=1}^{\infty} [C_{jn}\exp(n\mathrm{i}kx) + \overline{C}_{jn}\exp(-n\mathrm{i}kx)] \tag{62}$$

where

$$C_{jn} = \sum_{m=n}^{\infty} H_{jmn}(k,t)\eta_0^m,$$

and from (61), the H_{jmn} are known up to $n = 3$ and $m = 3$:

$$H_{j11} = \psi_{j1}, \quad H_{j21} = 0, \quad H_{j31} = \Psi_{j3},$$

$$H_{j22} = \psi_{j2}, \quad H_{j32} = 0, \quad H_{j33} = \psi_{j3},$$

and the ψ_{jm} are given earlier in (30), (46) and (55), and Ψ_{j3} is given in (56). The above Fourier series represents the distortion of the surface waves, and it is noticed that there does not exist a purely time-dependent series, as is the case for the nonlinear Rayleigh breakup of circular liquid jets (Yuen 1968). This is because for the present liquid sheets the mass of the liquid is always conserved for the sinusoidal surface deformation.

4. Results and discussion

A typical result of (61) is shown in figure 3 for the dimensionless surface deformation as a function of dimensionless distance for the dimensionless initial disturbance amplitude of 0.1, the Weber number of 40 and the gas-to-liquid density ratio of 10^{-3} which approximates the situation of liquid water in ambient air. The dimensionless wavenumber of 0.02 is almost equal to the dominant wavenumber for the sinuous disturbance of the linearized theory. It is seen that the surface wave grows in time, but remains sinusoidal and maintains its sinuous character for the majority of its growth time, the deviation from the linear theory is small, and the distance between the two interfaces is kept almost constant along the wavelength up to the dimensionless time of 1000. After that time, the nonlinear effect becomes significant and the wave form is distorted considerably. At $t = 1298$, the distance between the two interfaces vanishes near the half and full wavelength, which is different from the conclusions reached by

https://doi.org/10.1017/S0022112099007491 Published online by Cambridge University Press

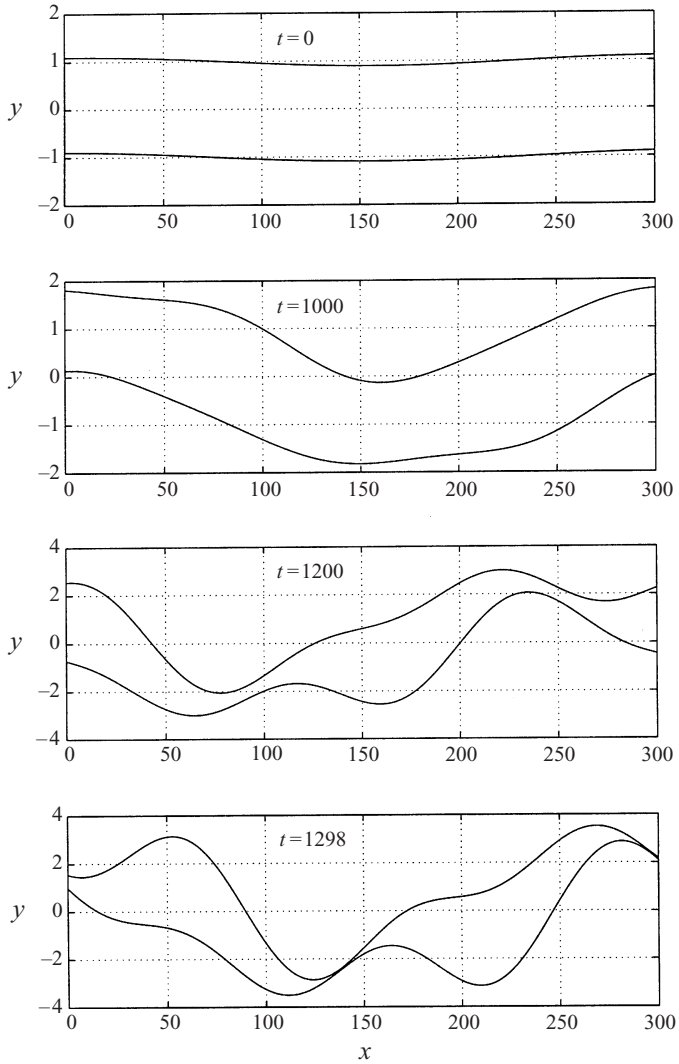


FIGURE 3. Evolution of the dimensionless surface deformation y as a function of dimensionless distance x for $We = 40$, $\rho = 0.001$, $k = 0.02$, and $\eta_0 = 0.1$. The dimensionless time t is specified on the figure.

Clark & Dombrowski (1972) who found that the sheet breakup occurred at positions corresponding to 3/8 and 7/8 of the length of the fundamental wave. However, the liquid sheet breaks off at half-wavelength intervals, a result consistent with that of Clark & Dombrowski (1972).

Figure 4 illustrates the effect of the fundamental, and the first and second harmonics on the evolution of the surface waves at the breakup time under the same conditions as those of figure 3. It is clear from figure 4(*a*) that the first-order (i.e. linearized) analysis does not lead to reasons as to why the liquid sheet breakup occurs or how the liquid sheet breaks up, because the two gas–liquid interfaces remain exactly the same distance apart as the wave grows temporally. However, the liquid sheet thinning and eventual breakup appear when the first harmonic is added onto the fundamental wave, as shown in figure 4(*b*), because the first harmonic is essentially a varicose disturbance that causes the pinch-off of the sheet at half-wavelength intervals. The

https://doi.org/10.1017/S0022112099007491 Published online by Cambridge University Press

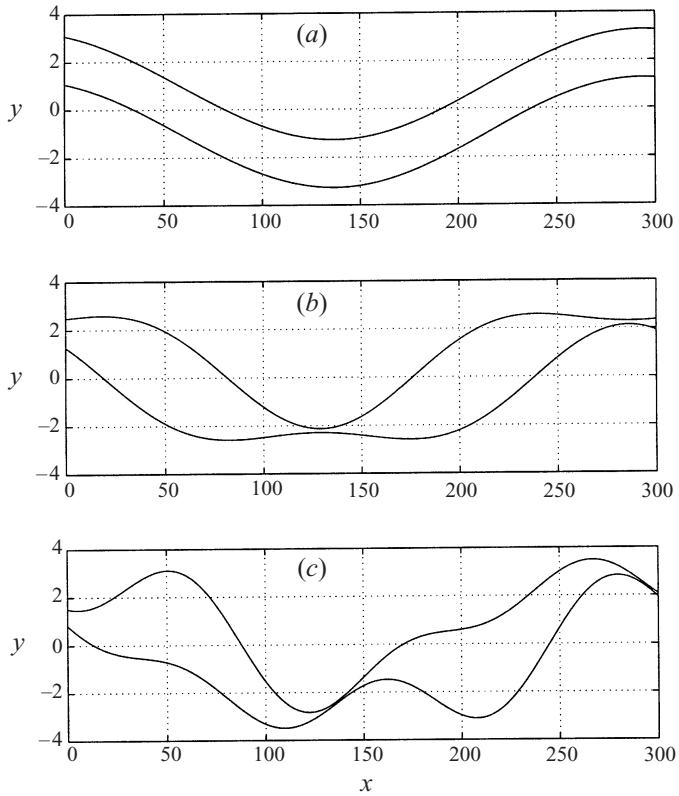


FIGURE 4. The effect of the fundamental, and the first and second harmonic on the dimensionless surface deformation y as a function of dimensionless distance x at the breakup time $t = 1298$ for $We = 40$, $\rho = 0.001$, $k = 0.02$, and $\eta_0 = 0.1$. (*a*) Fundamental; (*b*) fundamental plus the first harmonic; (*c*) fundamental plus the first and second harmonics.

surface wave shown in figure 4(*c*), where the first and second harmonics are included in addition to the fundmental, is significantly different from those shown in figures 4(*a*) and 4(*b*); in particular the occurrence of the sheet breakup is predicted in figure 4(*c*), which contrasts with the result shown in figure 4(*b*) where the sheet has not broken up. Therefore, as Bogy (1979) pointed out, it is necessary to include the analysis up to the third order, if the breakup length (or time) and features of the breakup details are required. This figure also indicates that the thinning of the sheet is caused by the growth of harmonic waves, and that the breakup occurs near the crests of each interface at the low density ratio of $\rho = 0.001$. These observations are in agreement with the previous results of Rangel & Sirignano (1991).

The behaviour of the liquid sheet and the surface wave growth for different flow conditions are qualitatively similar to those shown in figure 3, but an important difference occurs in the rate of growth of the disturbance, therefore the breakup time. Figure 5 shows the effects of the initial disturbance amplitude η_0 on the surface wave development for the Weber number of 40, density ratio of 10^{-3} and the wavenumber of 0.0204, which corresponds to the dominant wavenumber of the linearized theory. It is seen that as the initial disturbance amplitude is increased, the liquid sheet breaks up at earlier times, as expected. For example, the dimensionless breakup time is 2875 for $\eta_0 = 0.001$, and is only 815 when $\eta_0 = 0.3$. It is also observed that the positions at which the breakup occurs change as the initial amplitude is varied, although the

https://doi.org/10.1017/S0022112099007491 Published online by Cambridge University Press

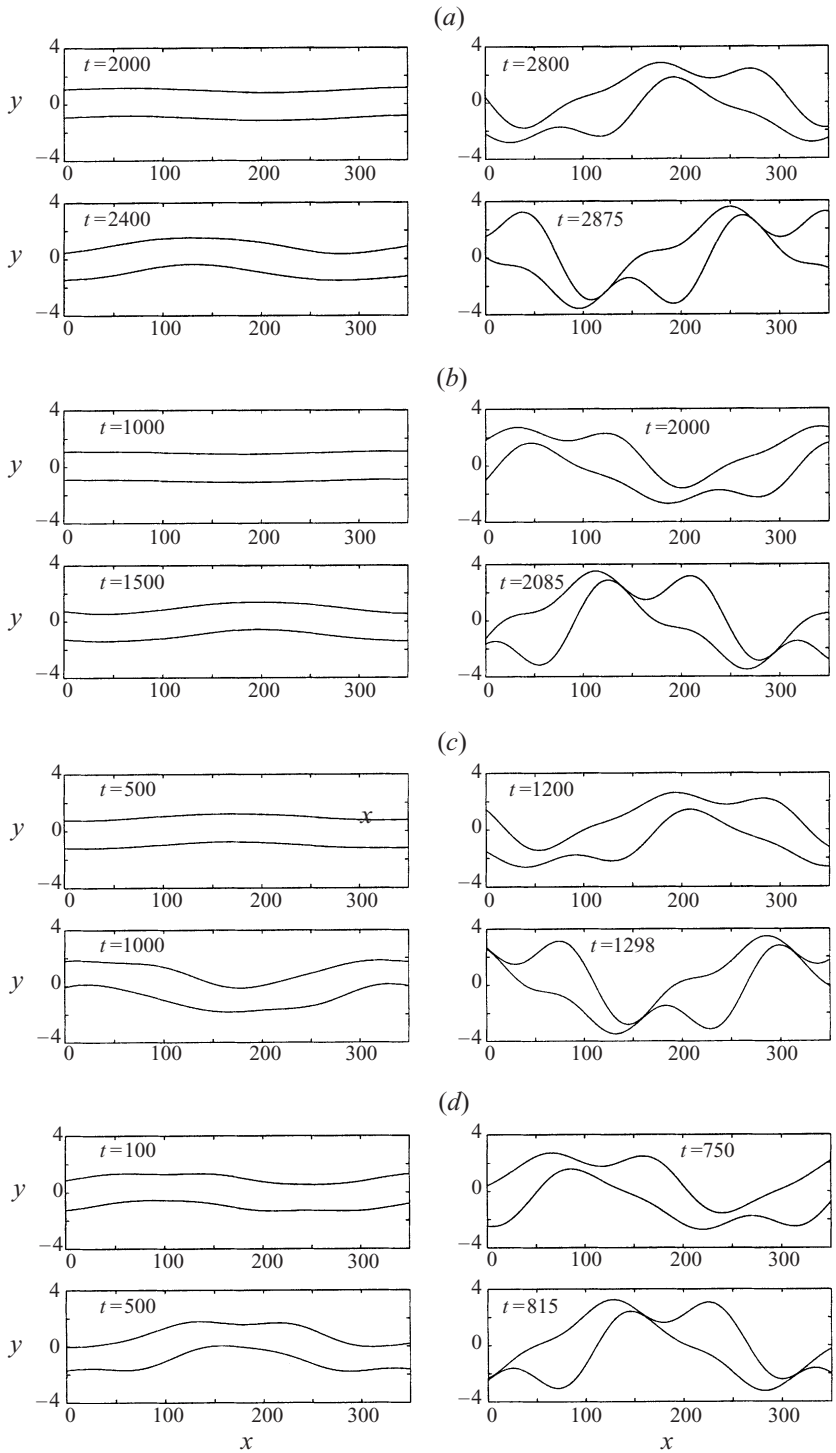


FIGURE 5. Evolution of the dimensionless surface deformation y as a function of dimensionless distance x at the dominant wavenumber of $k = 0.0204$ for $We = 40$ and $\rho = 0.001$. The initial amplitude η_0 is 0.001 (*a*); 0.01 (*b*); 0.1 (*c*); and 0.3 (*d*).

https://doi.org/10.1017/S0022112099007491 Published online by Cambridge University Press

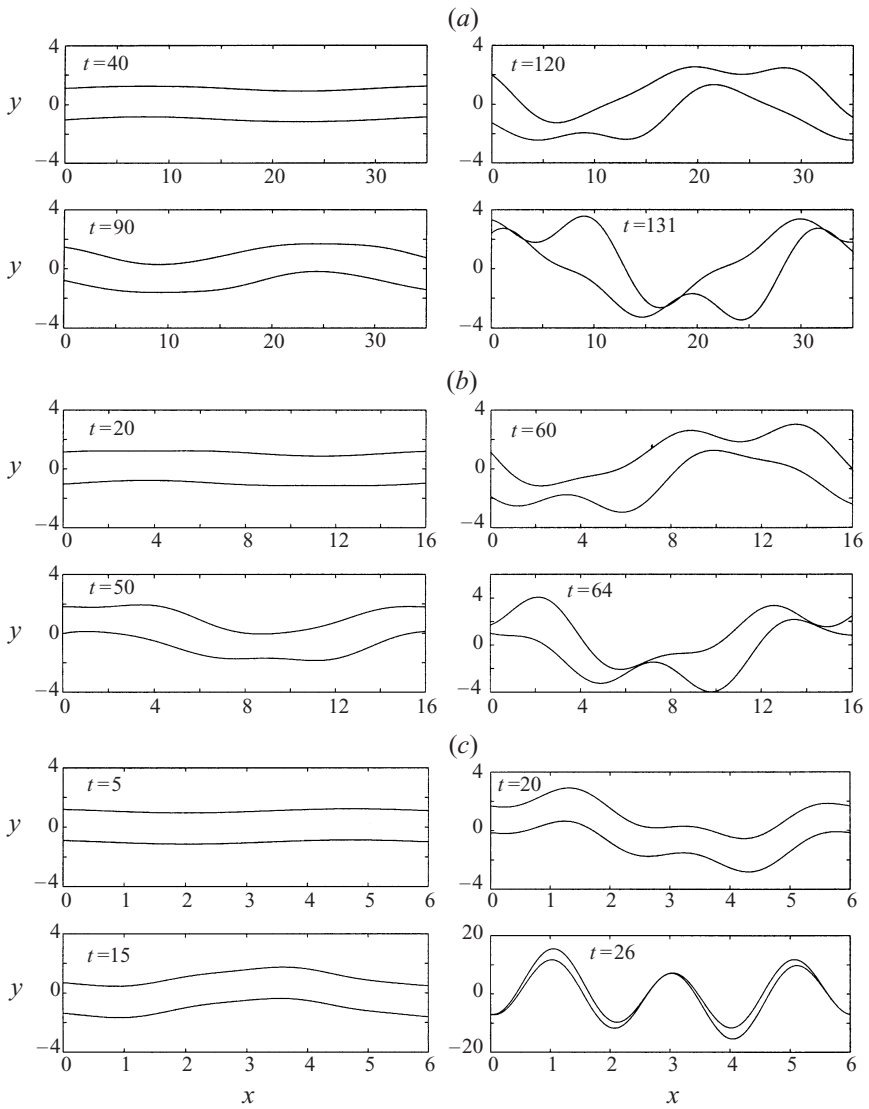


FIGURE 6. Evolution of the dimensionless surface deformation y as a function of dimensionless distance x at the respective dominant wavenumbers for $We = 40$, $\eta_0 = 0.1$, and the gas-to-liquid density ratio ρ of 0.01 (a); 0.02 (b); 0.05 (c). The case for $\rho = 0.001$ is given in figure 5(c).

breakup still occurs at the half-wavelength interval. It is also interesting to note that the wave amplitude at the sheet breakup is about the same for different values of η_0. Further, the nonlinear effect is clearly observable during the early part of the wave growth for the large value of $\eta_0 = 0.3$, whereas for the small values of η_0 (such as 0.001 shown in figure 5a) the linear theory is valid for a substantial amount of the growth time, up to the time $t = 2400$ which is over 83% of the breakup time, even though the wave amplitude is not that small compared to the sheet thickness.

The effect of the gas-to-liquid density ratio on the surface wave development is given in figure 6 for $We = 40$ and $\eta_0 = 0.1$. The wavenumber used for each value of the density ratio is the dominant wavenumber under the given conditions according to the linearized theory. The results for $\rho = 10^{-3}$ are given in figure 5(c), whereas

https://doi.org/10.1017/S0022112099007491 Published online by Cambridge University Press

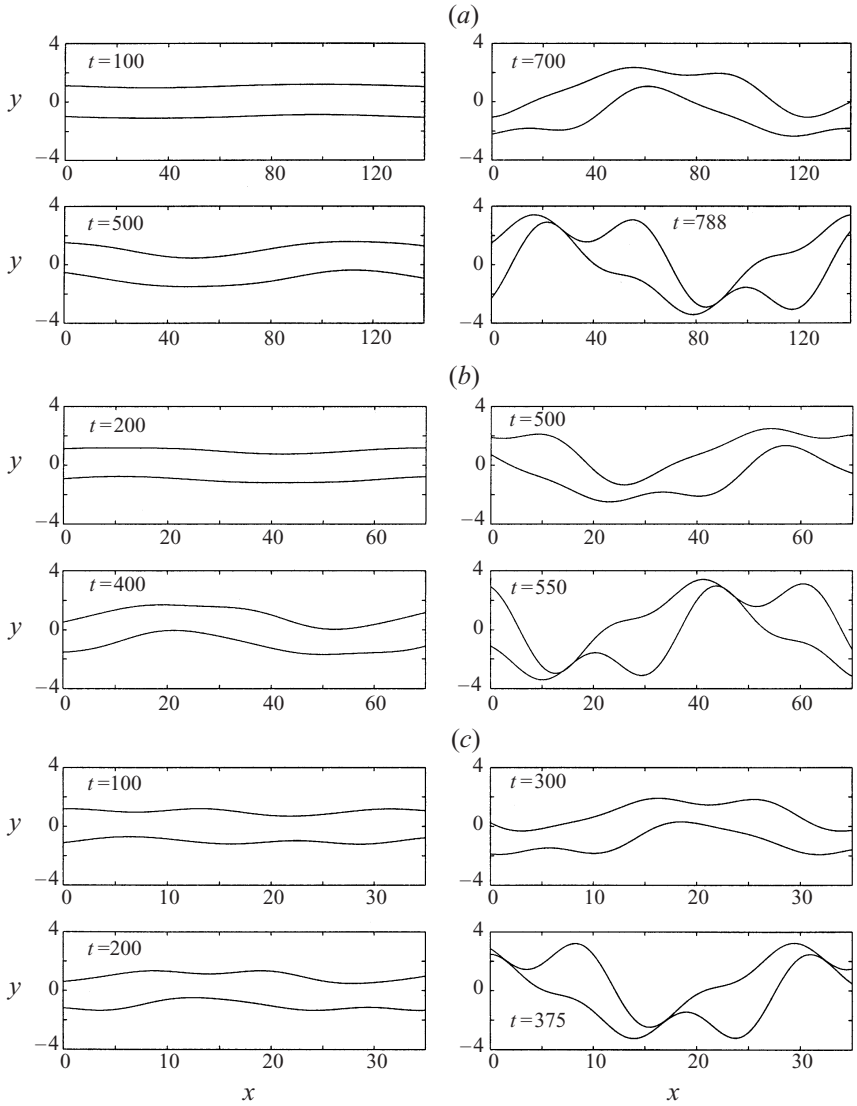


FIGURE 7. Evolution of the dimensionless surface deformation y as a function of dimensionless distance x at the respective dominant wavenumbers for $\rho = 0.001$, $\eta_0 = 0.1$, and the Weber number We of 100 (a); 200 (b); 400 (c). The case for $We = 40$ is given in figure 5(c).

figure 6(a–c) presents the results for $\rho = 0.01$, 0.02 and 0.05, respectively. As expected, the liquid sheet breaks up considerably earlier for density ratios of large values than for those of small values. It is also evident that the wave amplitude at the sheet breakup increases as the density ratio is increased; in particular the amplitude for $\rho = 0.05$ is nearly four times that of the lower values of the density ratio.

Figure 7 shows the effect of the Weber number on the liquid sheet deformation for $\rho = 0.001$ and $\eta_0 = 0.1$ with the case of $We = 40$ given in figure 5(c). Once again the wavenumber used is the dominant wavenumber of the linearized theory for the conditions given. It is observed that the breakup time is reduced as the Weber number is increased, agreeing with known experimental observations. At the Weber number of 400 shown in figure 7(c), the surface wave exhibits both sinusoidal and varicose

https://doi.org/10.1017/S0022112099007491 Published online by Cambridge University Press

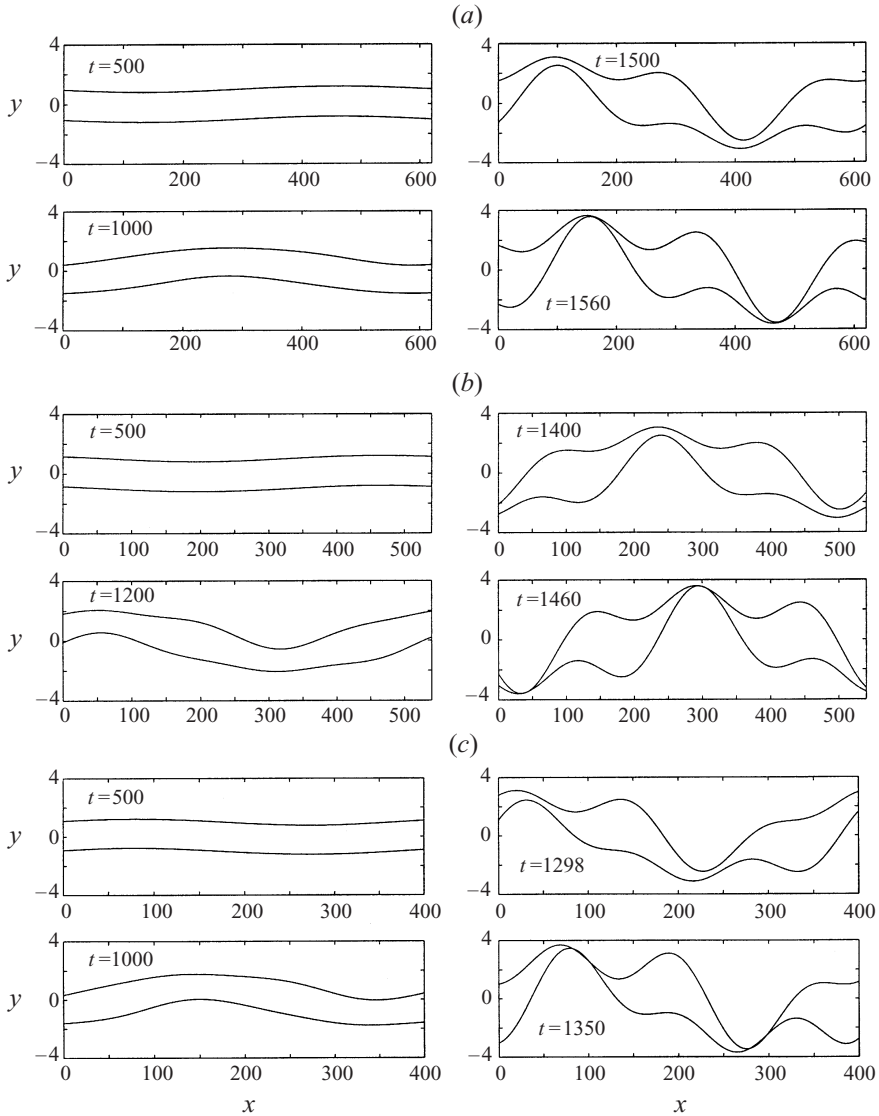


FIGURE 8. Evolution of the dimensionless surface deformation y as a function of dimensionless distance x for $We = 40$, $\rho = 0.001$, $\eta_0 = 0.1$, and the wavenumber k of 0.01 (a); 0.012 (b); 0.016 (c). The case responding to the dominant wavenumber ($k = 0.0204$) is given in figure 5(c).

deformation before the sheet breakup, which is clearly different from the cases of smaller Weber numbers shown in figures 5(c), 7(a, b), where the surface deformation is much more clearly sinuous for the majority of the wave development.

In the case of circular liquid jet breakup in the Rayleigh regime, one main drop and one or more usually smaller drops, referred to as the satellite or spherous drops, are formed, corresponding to each wavelength of an unstable disturbance. The satellite drop formation is particularly favoured for disturbances of long wavelengths (Yuen 1968; Rutland & Jameson 1971). Therefore, the effect of wavelength on the surface wave development is investigated, and typical results are presented in figure 8 for $We = 40$, $\rho = 10^{-3}$ and $\eta_0 = 0.1$. Under this condition, the dominant wavenumber of the linearized theory is equal to 0.0204, and the corresponding results have been given

https://doi.org/10.1017/S0022112099007491 Published online by Cambridge University Press

in figure 5(*c*). It is evident that the liquid sheet breakup occurs at half-wavelength intervals, as observed earlier, and this parcel of liquid is expected to contract into a ligament under the action of surface tension. There does not exist any indication of 'satellite' ligament formation from the liquid sheet breakup. This is because, for circular liquid jet breakup, the second-order term of the perturbation solution would cause the formation of the satellite drops (Yuen 1968), whereas sheet breakup, according to the present analysis, is due to the second-order term which is essentially varicose in nature, and the next higher-order term of varicose surface deformation is the fourth-order term, which is not included in the present analysis and might be too small in magnitude in reality to result in the 'satellite' ligament formation. Therefore, it would be interesting to consider the initial condition of the fundamental mode that includes both sinuous and varicose disturbances.

At this point, the good agreement between the linearized theory and Hagerty & Shea's (1955) as well as Crapper, Dombrowski & Pyott's (1975) experimental results for liquid sheet instability can be explained. Because the second-order term of the perturbation solution is varicose in nature, and it provides a mechanism for the liquid sheet thinning and eventual breakup, it does not contribute to the maximum sinusoidal deformation of the liquid sheet. Experimentally, sinuous waves are predominant, and the growth of sinuous waves has been determined by measuring the maximum surface deformation. Therefore, the correction from the linearized theory is only in the third order for this method of measurements. It might be concluded that for any growth of an initially sinuous disturbance, the above method of measurement would provide a reasonably accurate approach for the measurement of the linearized growth rate of the sinuous waves on plane liquid sheets.

In the present temporal instability analysis, temporal frequencies for the fundamental, and the first and second harmonics are treated as complex. That implies that surface waves grow in time everywhere along the sheet, as shown in figures 3–8. This is contrary to experimental observations (Li 1993). A more physically consistent analysis can be made in terms of spatial instability by treating the wavenumber as complex and the temporal frequency as real. The spatial instability is particularly appropriate in describing the instability of liquid sheets subjected to disturbances at the nozzle exit. Li (1993) shows that for Weber numbers much larger than unity, a situation typical of practical applications, the spatial instability of plane liquid sheets is related to the corresponding temporal instability through Gaster's transformation (Gaster 1962), and the phase velocity and group velocity of the surface waves are essentially equal to the liquid sheet velocity. Hence, the results of the present study may be transformed into the spatial instability. In the non-dimensional form the spatial distance and time become the same when a/U_l is used as the time scale and the half-sheet thickness a as the length scale, which is the case for the present study. As a result, the time required for the sheet to break up (or the breakup time) in the temporal analysis becomes equal numerically to the distance required for the sheet to disintegrate (or the so-called breakup length). By replacing the dimensionless time t in (61) by the dimensionless distance x from the nozzle exit, the present temporal development of the surface wave is transformed into the spatial evolution, and a typical result is shown in figure 9 for $We = 280.78$, $\rho = 0.00129$, and $k = 0.183$. The initial amplitude is varied from $\eta_0 = 0.01$ to 0.2, and the wavenumber of $k = 0.183$ corresponds to the dominant value of the linear theory. It is seen that the wave develops at the nozzle exit, and its amplitude increases downstream. Although the wave remains sinuous for most of the sheet length, nonlinear effects cause the sheet thinning and pinching that lead to the eventual breakup of the sheet. As the initial

https://doi.org/10.1017/S0022112099007491 Published online by Cambridge University Press

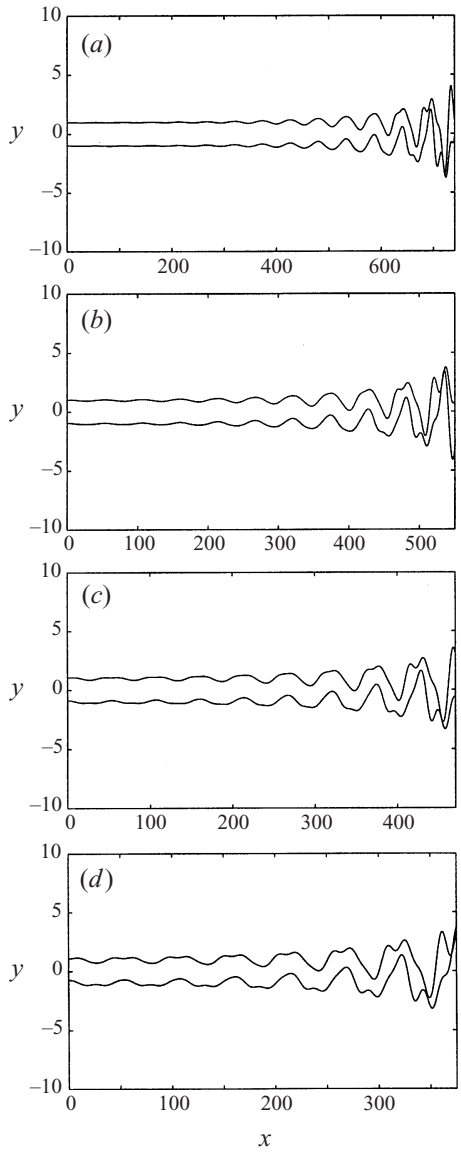


FIGURE 9. Spatial surface deformation for $We = 280.78$, $\rho = 0.00129$, $k = 0.183$ and $\eta_0 = 0.01$ (a); 0.05 (b); 0.1 (c) and 0.2 (d).

disturbance amplitude η_0 is increased, the sheet distortion due to the nonlinear effects becomes more pronounced and appears much closer to the nozzle exit, and the sheet breakup length is reduced. Also the wave amplitude at the breakup point decreases slightly with increasing initial disturbance amplitude. The results clearly show that thinning of the liquid sheet occurs as a result of the growth of the first harmonic which acts as a varicose wave with its wavelength equal to half of the fundamental.

In practical applications, the breakup time (or length) is of significant importance because it indicates the region where the sheet disintegration and droplet formation occurs. This knowledge is particularly important for numerical simulations of spray systems. Figure 10 shows the breakup time as a function of the wavenumber for different initial disturbance amplitudes under the condition of $We = 40$ and $\rho =$

https://doi.org/10.1017/S0022112099007491 Published online by Cambridge University Press

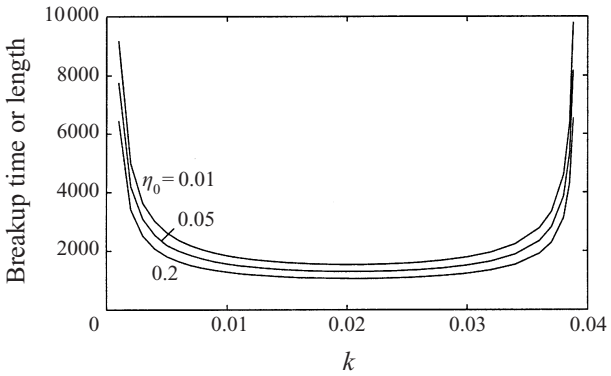


FIGURE 10. The effect of the wavenumber on the liquid sheet breakup time (or length) for different initial amplitudes of disturbance η_0. $We = 40$, $\rho = 0.001$ and $\eta_0 = 0.01,\ 0.05,\ 0.2$, respectively.

10^{-3}. As observed earlier, the breakup time first decreases for each initial amplitude η_0 until reaching a minimum value and then increases towards infinity when the wavenumber approaches the cut-off wavenumber k_c. This is because the surface waves become stable for wavenumbers $\leqslant 0$ and $\geqslant k_c$, corresponding to infinitely long breakup time. It is also seen that the breakup-time curve is almost flat for a significant region of the unstable wavenumbers including the dominant wavenumber, suggesting that the breakup time (or length) does not change significantly with the disturbance wavelength. Further, the present results show that a larger initial disturbance amplitude results in shorter breakup time, as expected. For the purpose of comparison, it should be emphasized that the linear stability analysis yields infinitely large breakup time, as discussed in the Introduction section.

The effect of the Weber number on the breakup time (length) is shown in figure 11 for several values of initial disturbance amplitude and two values of the density ratio ρ. It is clear that the breakup time decreases as the Weber number is increased. This is because the higher the Weber number, the larger the aerodynamic interactions between the liquid sheet and the surrounding gas, and the latter is responsible for the growth of the surface waves and the eventual disintegration of the sheet. However, for small Weber numbers, the reduction in the breakup time is very rapid as We is increased, and then the decrease in the breakup time becomes very gradual for large Weber numbers. This might explain why the breakup length changes little for different flow conditions under practical operating conditions of large We. It is also shown that the breakup time is reduced by a larger value of the initial disturbance amplitude and the density ratio. More details are shown in figure 12 for the effect of the gas-to-liquid density ratio on the breakup time. It is seen that the breakup time is reduced significantly for an increase in the density ratio when ρ is small, and then it almost approaches an asymptotic value for larger values of ρ. This suggests that for practical situations such as in aircraft engines where the combustor chamber pressure is high (ranging from 20 to 30 atm.), the breakup length might be taken as an invariant regardless of the magnitudes of fluctuations in the flow conditions.

Figure 13 shows the effect of the initial amplitude of the disturbance on the breakup time of the liquid sheet. The vertical coordinate is linear, while the horizontal coordinate is on the logarithmic scale. The results indicate that increasing the initial amplitude of the disturbance reduces the breakup time significantly, as pointed out earlier. For the small values of η_0 shown in the figure, the dependence of the breakup time on η_0 is nearly logarithmic, because the linearized theory is valid for the majority

https://doi.org/10.1017/S0022112099007491 Published online by Cambridge University Press

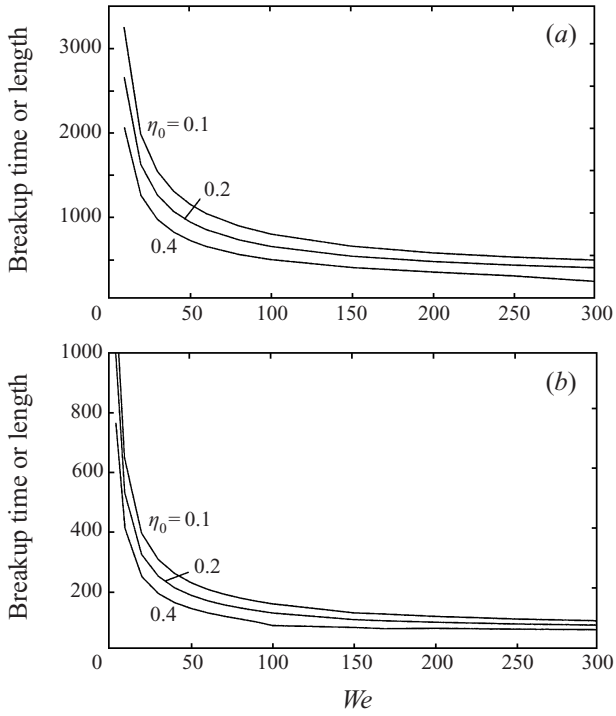


FIGURE 11. The effect of the Weber number on the breakup time (length) for several initial amplitudes of disturbance. $\eta_0 = 0.1,\ 0.2$, and 0.4, respectively, and $\rho = 0.001$ (*a*); 0.005 (*b*).

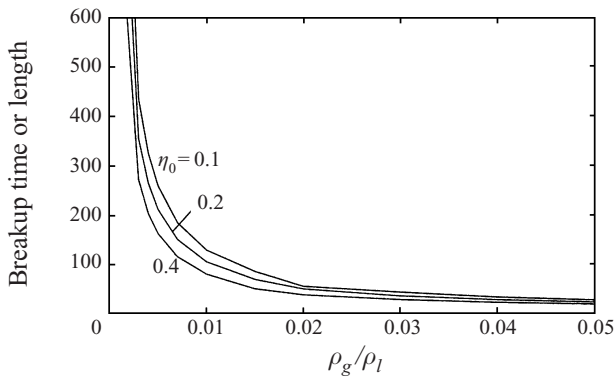


FIGURE 12. The effect of the gas-to-liquid density ratio on the breakup time (length) for several initial amplitudes of disturbance. $We = 40$ and $\eta_0 = 0.1,\ 0.2$, and 0.4, respectively.

of the wave growth history. The deviation from the logarithmic dependence (i.e. the linearized theory) increases for larger values of η_0. This can be seen more clearly by plotting the wave amplitude over time for both linearized and the present third-order theory, as shown in figure 14. For all the results presented in this figure, the wavenumber for the maximum growth predicted by the linearized theory is used, and the curves end at the sheet breakup time. The solid curves represent the results for the linearized theory, and the dashed curves are the results for the present third-order theory. As expected, the linearized results are valid, strictly speaking, only for a brief time following the onset of the disturbance. Then the amplitude growth becomes

https://doi.org/10.1017/S0022112099007491 Published online by Cambridge University Press

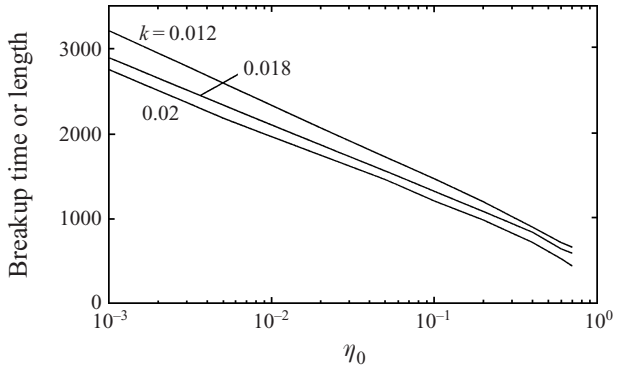


FIGURE 13. The effect of the initial disturbance amplitude on the breakup time (length) for $We = 40,\ \rho = 0.001$ and $k = 0.012,\ 0.018$, and 0.02, respectively.

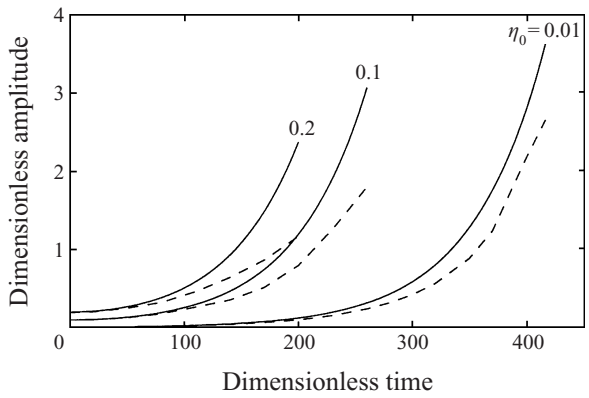


FIGURE 14. The effect of the initial disturbance amplitude on the growth of the wave amplitude. $We = 40,\ \rho = 0.005$ and $\eta_0 = 0.01,\ 0.1$, and 0.2, respectively. The solid curves: linearized results; the dashed curves: present nonlinear results. The curves end at the sheet breakup time.

gradually less than the exponential rate predicted by the linear theory. For large values of η_0 (such as 0.1 and 0.2 shown in the figure), the difference between the linear and nonlinear results are significant close to the breakup point, and the difference increases with η_0. However, for small values of η_0 (such as 0.01 or smaller) the linear theory is valid for a significant portion of the wave growth history, and becomes essentially valid even close to the breakup point for smaller initial amplitude of disturbances. As pointed out earlier, the wave amplitude at the breakup point decreases as the initial amplitude is increased. The breakup time has been calculated for a more broad range of various parameters, and has been correlated as a function of the Weber number, the density ratio and the initial disturbance amplitude, and the correlation has been used for the modelling of liquid atomization and sprays (Mitra & Li 1999).

5. Conclusions

Nonlinear effects on the instability and consequent breakup process of plane liquid sheets moving in an inviscid and incompressible gas medium at rest have been investigated by a perturbation expansion technique with the initial amplitude

https://doi.org/10.1017/S0022112099007491 Published online by Cambridge University Press

of the disturbance as the perturbation parameter. The first-, second- and third-order governing equations have been derived along with appropriate initial and boundary conditions which describe the characteristics of the fundamental, the first and second harmonics, and solutions up to the third order in the initial amplitude of the disturbance have been obtained for an initially sinusoidal sinuous surface disturbance. The results indicate that the thinning and subsequent breakup of liquid sheets are due to nonlinear effects with the generation of higher harmonics as well as feedback into the fundamental. In particular, the first harmonic of the fundamental sinuous mode is a varicose wave that leads to the pinching and eventual breakup of the liquid sheet at half-wavelength intervals of the fundamental wave, and it contributes little to the sinuous deformation of the liquid sheets. The contribution to the sinuous surface deformation is due to the fundamental with a correction arising from the third-order solution. Therefore, the good agreement, reported in the literature, between the growth rates predicted by the linearized theory and experimental results is due to the particular method of measurements employed, i.e. through the measurements of the maximum surface deformation. The breakup time (or length) of the liquid sheet is calculated, and the effect of the various flow parameters is investigated. It is found that the breakup time (or length) is reduced by an increase in the initial amplitude of disturbance, the Weber number and the gas-to-liquid density ratio, and it becomes asymptotically insensitive to the variations of the Weber number and the density ratio when their values become very large. It is also found that the breakup time (or length) is a very weak function of the wavenumber unless it is close to the cut-off wavenumbers.

This work was supported by the Natural Sciences and Engineering Research Council of Canada (NSERC).

Appendix A

$$A_{g2}(t) = -\frac{1}{4}\left[(\alpha_1^2 - \beta_1^2)t + \left(\frac{3\beta_1^2 + \alpha_1^2}{2\beta_1}\right)\sinh(2\beta_1 t)\right],$$

$$A_{l2}(t) = \frac{1}{4}[\beta_1^2 - (\alpha_1 + k)^2]\left(\frac{1 + \tanh^2(k)}{2}\right)t + \frac{1}{4}\left[-\beta_1\left(\frac{5 + \tanh^2(k)}{4}\right) - \frac{(\alpha_1 + k)^2}{\beta_1}\frac{1 + \tanh^2(k)}{4}\right]\sinh(2\beta_1 t),$$

$$A_1 = \frac{C}{(\omega_2 - \overline{\omega}_2)(\omega_2 - 2\overline{\omega}_1)} + \frac{\overline{C}}{(\omega_2 - \overline{\omega}_2)(\omega_2 - 2\omega_1)} + \frac{E}{(\omega_2 - \overline{\omega}_2)(\omega_2 - 2\alpha_1)},$$

$$A_2 = \frac{\overline{C}}{(\overline{\omega}_2 - 2\omega_1)(\omega_2 - 2\omega_1)}, \quad A_3 = \frac{E}{(\omega_2 - 2\alpha_1)(\overline{\omega}_2 - 2\alpha_1)},$$

$$C = -\tfrac{1}{32}[(\tanh^2(k) + 4\coth(2k)\tanh(k) - 5)(\overline{\omega}_1^2 + 2k\overline{\omega}_1 + k^2)],$$

$$E = -\tfrac{1}{16}\{(k^2 + 2k\alpha_1)[\tanh^2(k) + 4\coth(2k)\tanh(k) - 5] + 2(\beta_1^2 + \alpha_1^2)[\tanh(k)\coth(2k) + \tfrac{1}{2}\tanh^2(k) - \tfrac{3}{2}] - 2(\beta_1^2 - \alpha_1^2)[\tanh(k)\coth(2k) - 1]\}.$$

https://doi.org/10.1017/S0022112099007491 Published online by Cambridge University Press

Appendix B.

$$a_{31} = \Psi_{j3,t} + \mathrm{i}k\Psi_{j3} - k^2\tanh(k)\psi_{j2}\left(\frac{\overline{\psi}_{j1,t}}{k} - \mathrm{i}\overline{\psi}_{j1}\right)$$
$$-k^3\left[\overline{\psi}_{j1}(\psi_{j1}\psi_{j1,t} + \mathrm{i}\psi_{j1}^2) - \tfrac{1}{2}\psi_{j1}^2\left(\frac{\overline{\psi}_{j1,t}}{k} - \mathrm{i}\overline{\psi}_{j1}\right)\right]$$
$$+k\coth(2k)\left[2k^2\tanh(k)\overline{\psi}_{j1}\psi_{j1}\left(\frac{\psi_{j1,t}}{k} + \mathrm{i}\psi_{j1}\right) + \psi_{j2,t}\overline{\psi}_{j1} + 2\mathrm{i}k\overline{\psi}_{j1}\psi_{j2}\right] \quad (j=2),$$

$$a_{33} = \psi_{j3,t} + 3\mathrm{i}k\psi_{j3} + 3k^2\tanh(k)\psi_{j2}\left(\frac{\psi_{j1,t}}{k} + \mathrm{i}\psi_{j1}\right) - \frac{3k^3}{2}\psi_{j1}^2\left(\frac{\psi_{j1,t}}{k} + \mathrm{i}\psi_{j1}\right)$$
$$+3k\coth(2k)\left[2k^2\tanh(k)\psi_{j1}^2\left(\frac{\psi_{j1,t}}{k} + \mathrm{i}\psi_{j1}\right) + \psi_{j2,t}\psi_{j1} + 2\mathrm{i}k\psi_{j2}\psi_{j1}\right] \quad (j=2),$$

$$b_{31} = \Psi_{j3,t} - k\psi_{j2}\overline{\psi}_{j1,t} + k\overline{\psi}_{j1}\psi_{j2,t} + k^2\psi_{j1}\overline{\psi}_{j1}\psi_{j1,t} + \frac{k^2}{2}\psi_{j1}^2\overline{\psi}_{j1,t},$$

$$b_{33} = \psi_{j3,t} + 3k\psi_{j2}\psi_{j1,t} + 3k\psi_{j1}\psi_{j2,t} + \frac{9k^2}{2}(\psi_{j1}^2\psi_{j1,t}),$$

$$D_1 = -\frac{1}{\omega_3 - \overline{\omega}_3}[D_2(\omega_1+\omega_2-\overline{\omega}_3) + D_3(\omega_1+\overline{\omega}_2-\overline{\omega}_3) + D_4(2\overline{\omega}_1+\omega_1-\overline{\omega}_3)$$
$$+D_5(3\omega_1-\overline{\omega}_3) + D_6(\omega_1+2\alpha_1-\overline{\omega}_3) + \overline{D}_2(\overline{\omega}_1+\overline{\omega}_2-\overline{\omega}_3) + \overline{D}_3(\overline{\omega}_1+\omega_2-\overline{\omega}_3)$$
$$+\overline{D}_4(2\omega_1+\overline{\omega}_1-\overline{\omega}_3) + \overline{D}_5(3\overline{\omega}_1-\overline{\omega}_3) + \overline{D}_6(\overline{\omega}_1+2\alpha_1-\overline{\omega}_3)],$$

$$D_2 = \frac{A_1}{4(\overline{\omega}_1+\omega_2-\omega_3)(\omega_1+\omega_2-\overline{\omega}_3)}(\omega_1^2B_1 + \omega_2^2B_2 + \omega_1\omega_2B_3 - \mathrm{i}\omega_2B_6 - \mathrm{i}\omega_1B_7 - B_{10}),$$

$$D_3 = \frac{\overline{A}_1}{4(\omega_1+\overline{\omega}_2-\omega_3)(\omega_1+\overline{\omega}_2-\overline{\omega}_3)}(\omega_1^2B_1 + \overline{\omega}_2^2B_2 + \omega_1\overline{\omega}_2B_3 - \mathrm{i}\overline{\omega}_2B_6 - \mathrm{i}\omega_1B_7 - B_{10}),$$

$$D_4 = \frac{1}{(\omega_1+2\overline{\omega}_1-\omega_3)(\omega_1+2\overline{\omega}_1-\overline{\omega}_3)}\left[\tfrac{1}{64}(\overline{\omega}_1^2B_4 + \omega_1^2B_5 - \mathrm{i}\omega_1B_8 - B_9)\right.$$
$$\left.+\frac{\overline{A}_2}{4}(\omega_1^2B_1 + 4\overline{\omega}_1^2B_2 + 2\omega_1\overline{\omega}_1B_3 - 2\mathrm{i}\overline{\omega}_1B_6 - \mathrm{i}\omega_1B_7 - B_{10})\right],$$

$$D_5 = \frac{1}{(2\omega_1-\omega_3)(3\omega_1-\overline{\omega}_3)}\left[\tfrac{1}{64}(\omega_1^2B_4 + \omega_1^2B_5 - \mathrm{i}\omega_1B_8 - B_9)\right.$$
$$\left.+\frac{A_2}{4}(\omega_1^2B_1 + 4\omega_1^2B_2 + 2\omega_1^2B_3 - 2\mathrm{i}\omega_1B_6 - \mathrm{i}\omega_1B_7 - B_{10})\right],$$

$$D_6 = \frac{1}{(\omega_1+2\alpha_1-\omega_3)(\omega_1+2\alpha_1-\overline{\omega}_3)}\left[\tfrac{1}{64}(2\omega_1\overline{\omega}_1B_4 + 2\omega_1^2B_5 - 2\mathrm{i}\omega_1B_8 - 2B_9)\right.$$
$$\left.+\frac{A_3}{4}(\omega_1^2B_1 + 4\alpha_1^2B_2 + 2\alpha_1\omega_1B_3 - 2\mathrm{i}\alpha_1B_6 - \mathrm{i}\omega_1B_7 - B_{10})\right],$$

$$B_1 = 1 - \tanh(k)\tanh(3k), \quad B_2 = 1 - \tanh(3k)\coth(2k),$$
$$B_3 = 3 - \tanh(k)\coth(2k) - \tanh(k)\tanh(3k) - \tanh(3k)\coth(2k),$$
$$B_4 = 6k\tanh(k) - 4k\tanh(k)\coth(2k)\tanh(3k) + k\tanh(3k) + \rho k$$
$$-2k\tanh^{2}(k)\coth(2k),$$

https://doi.org/10.1017/S0022112099007491 Published online by Cambridge University Press

$$B_5 = \frac{3k}{2}\tanh(k) + \frac{k}{2}\tanh(3k) - 2k\tanh(k)\coth(2k)\tanh(3k),$$
$$B_6 = -\mathrm{i}k[-7 + \tanh(k)\tanh(3k) + 5\tanh(3k)\coth(2k) + \tanh(k)\coth(2k)],$$
$$B_7 = -2\mathrm{i}k[2\tanh(k)\tanh(3k) + \tanh(3k)\coth(2k) + \tanh(k)\coth(2k) - 4],$$
$$B_8 = \mathrm{i}k^2[-12\tanh(k)\coth(2k)\tanh(3k) + 3\tanh(3k) + 15\tanh(k) - 4\tanh^2(k)\coth(2k)],$$
$$B_9 = \frac{k^3}{2}\left[4\tanh^2(k)\coth(2k) - 15\tanh(k) + 12\tanh(k)\coth(2k)\tanh(3k) - 3\tanh(3k) - \frac{3k}{We}\right],$$
$$B_{10} = k^2[2\tanh(k)\coth(2k) + 3\tanh(k)\tanh(3k) + 6\tanh(3k)\coth(2k) - 11],$$

$$F_1 = -\frac{1}{\omega_1 - \overline{\omega}_1}[(\omega_2 - \omega_1 - \overline{\omega}_1)F_2 + (\overline{\omega}_2 - 2\overline{\omega}_1)\overline{F}_2 + (\omega_2 - 2\overline{\omega}_1)F_3 + (\overline{\omega}_2 - \omega_1 - \overline{\omega}_1)\overline{F}_3 + 2(\omega_1 - \overline{\omega}_1)F_4 + (\overline{\omega}_1 - \omega_1)\overline{F}_4 + (\omega_1 - 2\overline{\omega}_1)F_5 - \omega_1\overline{F}_5 + (2\alpha_1 - \omega_1 - \overline{\omega}_1)F_6 + (\alpha_1 - \overline{\omega}_1)\overline{F}_6],$$
$$F_2 = \frac{A_1}{4(\omega_2 - 2\omega_1)(\omega_2 - \omega_1 - \overline{\omega}_1)}(\omega_1^2 G_1 + \omega_2^2 G_2 - \omega_1\omega_2 G_7 - \mathrm{i}\omega_2 G_8 + \mathrm{i}\omega_1 G_9 - G_{15}),$$
$$F_3 = \frac{A_1}{4(\omega_2 - 2\overline{\omega}_1)(\omega_2 - \omega_1 - \overline{\omega}_1)}(\overline{\omega}_1^2 G_1 + \omega_2^2 G_2 - \overline{\omega}_1\omega_2 G_7 - \mathrm{i}\omega_2 G_8 + \mathrm{i}\overline{\omega}_1 G_9 - G_{15}),$$
$$F_4 = \frac{1}{8(\omega_1 - \overline{\omega}_1)^2}(\overline{\omega}_1^2 G_1 A_2 + 4\omega_1^2 G_2 A_2 + \tfrac{1}{16}\omega_1\overline{\omega}_1 G_3 + \tfrac{1}{16}\omega_1^2 G_4 + \tfrac{1}{16}\omega_1^2 G_5 + \tfrac{1}{16}\overline{\omega}_1^2 G_6 - 2\omega_1\overline{\omega}_1 G_7 A_2 - 2\mathrm{i}\omega_1 G_8 A_2 + \mathrm{i}\overline{\omega}_1 G_9 A_2 + \tfrac{1}{16}\mathrm{i}\overline{\omega}_1 G_{10} + \tfrac{1}{16}\mathrm{i}\omega_1 G_{11} - \tfrac{1}{16}G_{14} - A_2 G_{15}),$$
$$F_5 = \frac{1}{16\overline{\omega}_1(2\overline{\omega}_1 - \omega_1)}(\overline{\omega}_1^2 G_{12} + \mathrm{i}\overline{\omega}_1 G_{13}),$$
$$F_6 = \frac{1}{8(\alpha_1 - \omega_1)(2\alpha_1 - \omega_1 - \overline{\omega}_1)}(\omega_1^2 G_1 A_3 + 4\alpha_1^2 G_2 A_3 + \tfrac{2}{16}\omega_1\overline{\omega}_1 G_4 - 2\alpha_1\omega_1 G_7 A_3 - 2\mathrm{i}\alpha_1 G_8 A_3 + \mathrm{i}\omega_1 G_9 A_3 + \tfrac{2}{16}\mathrm{i}\omega_1 G_{10} - \tfrac{2}{16}G_{14} - A_3 G_{15}),$$
$$F_7 = -\frac{1}{16\omega_1\overline{\omega}_1}[(\omega_1^2 + \overline{\omega}_1^2)G_{12} + \mathrm{i}(\omega_1 + \overline{\omega}_1)G_{13}],$$

$$G_1 = \tanh^2(k) - 2\rho + 1, \quad G_2 = 1 - \tanh(k)\coth(2k),$$
$$G_3 = 2\rho k - 3\tanh(k) + k^2\tanh(k), \quad G_4 = -\rho k + k^2\tanh(k) - 2k\tanh^2(k)\coth(2k),$$
$$G_5 = k\tanh(k) + k^2\tanh(k) - 2k\tanh^2(k)\coth(2k),$$
$$G_6 = -\rho k + \frac{k^2}{2}, \quad G_7 = -4\rho + 2 + \tanh^2(k),$$
$$G_8 = \mathrm{i}k[2 - 3\tanh(k)\coth(2k) - \tanh(k) - \tanh^2(k)],$$
$$G_9 = 4\mathrm{i}k + 4\mathrm{i}k^3\tanh^2(k)\coth(2k) + 2k^2\tanh(k)\coth(2k) - 2\mathrm{i}k\tanh(k)\coth(2k),$$
$$G_{10} = -\tfrac{1}{2}\mathrm{i}k^2\tanh(k),$$
$$G_{11} = \mathrm{i}[7k^2\tanh(k) - 4k^2\tanh^2(k)\coth(2k) - 2\tanh(k)\coth(2k) + k^3\tanh(k)],$$

https://doi.org/10.1017/S0022112099007491 Published online by Cambridge University Press

$$G_{12} = -\frac{k}{2}\tanh(k), \quad G_{13} = \frac{\mathrm{i}k^2}{2}\tanh(k),$$

$$G_{14} = 4k^3\tanh^2(k)\coth(2k) + 2\mathrm{i}k^3\tanh(k) - 2k^3\tanh(k) + \frac{3k^2}{2We},$$

$$G_{15} = k^2 + k^2\tanh^2(k) + 2k^2\tanh(k)\coth(2k).$$

REFERENCES

Asare, H. R., Takahashi, R. K. & Hoffman, M. A. 1981 Liquid sheet jet experiments: Comparison with linear theory. *Trans. ASME*: *J. Fluids Engng* **103**, 595–604.

Ashgriz, N. & Mashayek, F. 1995 Temporal analysis of capillary jet breakup. *J. Fluid Mech.* **291**, 163–190.

Bogy, D. B. 1978 Use of one-dimensional Cosserat theory to study instability in a viscous liquid jet. *Phys. Fluids* **21**, 190–197.

Bogy, D. B. 1979 Drop formation in a circular liquid jet. *Ann. Rev. Fluid Mech.* **11**, 207–228.

Cao, J. & Li, X. 1999 Stability of plane liquid sheets in compressible gas streams. *AIAA J. Propulsion Power*. Accepted for publication.

Clark, C. J. & Dombrowski, N. 1972 Aerodynamic instability and disintegration of inviscid liquid sheets. *Proc. R. Soc. Lond.* A **329**, 467–478.

Crapper, G. D., Dombrowski, N. & Pyott, G. A. D. 1975 Large amplitude Kelvin–Helmholtz waves on thin liquid sheets. *Proc. R. Soc. Lond.* A **342**, 209–224.

Gaster, M. 1962 A note on the relation between temporally-increasing and spatially-increasing disturbances in hydrodynamic stability. *J. Fluid Mech.* **14**, 222–224.

Hagerty, W. W. & Shea, J. F. 1955 A study of the stability of plane fluid sheets. *Trans. ASME: J. Appl. Mech.* **22**, 509–514.

Hashimoto, H. & Suzuki, T. 1991 Experimental and theoretical study of fine interfacial waves on thin liquid sheet. *JSME Intl J.* II **34**, 277–283.

Lefebvre, A. H. 1983 *Gas Turbine Combustion*. McGraw-Hill.

Lefebvre, A. H. 1989 *Atomization and Sprays*. Hemisphere.

Li, X. 1993 Spatial instability of plane liquid sheets. *Chem. Engng Sci.* **48**, 2973–2981.

Li, X. 1994 On the instability of plane liquid sheets in two gas streams of unequal velocities. *Acta Mechanica* **106**, 137–156.

Li, X. 1996 Spatial instability of plane liquid sheets. In *Mixed-Flow Hydrodynamics* (ed. N. P. Cheremisinoff), Chap. 7, pp. 145–166. Advances in Engineering Fluid Mechanics Series, Gulf Publishing Co.

Li, H. S. & Kelly, R. E. 1992 The instability of a liquid jet in a compressible airstream. *Phys. Fluids* A **4**, 2162–2168.

Li, X. & Tankin, R. S. 1991 On the temporal instability of a two-dimensional viscous liquid sheet. *J. Fluid Mech.* **226**, 425–443.

Lin, S. P. & Ibrahim, E. A. 1990 Stability of a viscous liquid jet surrounded by a viscous gas in a vertical pipe. *J. Fluid Mech.* **218**, 641–658.

Lin, S. P., Lian, Z. W. & Creighton, B. J. 1990 Absolute and convective instability of a liquid sheet. *J. Fluid Mech.* **220**, 673–689.

Mansour, A. & Chigier, N. 1990 Disintegration of liquid sheets. *Phys. Fluids* A **2**, 706–719.

Masters, K. 1985 *Spray Drying Handbook*, 4th edn. John Wiley.

Mitra, S. K. & Li, X. 1999 A predictive model for droplet size distributions in sprays. *Atomization and Sprays* **9**, 29–50.

Rangel, R. H. & Sirignano, W. A. 1988 Nonlinear growth of Kelvin–Helmholtz instability: Effect of surface tension and density Ratio. *Phys. Fluids* **31**, 1845–1855.

Rangel, R. H. & Sirignano, W. A. 1991 The linear and nonlinear shear instability of a fluid sheet. *Phys. Fluids* A **3**, 2392–2400.

Rutland, D. F. & Jameson, G. J. 1971 A non-linear effect in the capillary instability of liquid jets. *J. Fluid Mech.* **46**, 267–271.

https://doi.org/10.1017/S0022112099007491 Published online by Cambridge University Press

Spielbauer, T. M. & Aidun, C. K. 1994 The wave-thinning and breakup of liquid sheets. *Trans. ASME: J. Fluids Engng* **116**, 728–734.

Squire, H. B. 1953 Investigation of the instability of a moving liquid film. *Brit. J. Appl. Phys.* **4**, 167–169.

Taub, H. H. 1976 Investigation of nonlinear waves on liquid jets. *Phys. Fluids* **19**, 1124–1129.

Yuen, M. C. 1968 Nonlinear capillary instability of a liquid jet. *J. Fluid Mech.* **33**, 151–163.

https://doi.org/10.1017/S0022112099007491 Published online by Cambridge University Press